Shear heating-induced thermal pressurization during earthquake nucleation

S. V. Schmitt,[1] P. Segall,[1] and T. Matsuzawa[2]

Received 3 October 2010; revised 2 March 2011; accepted 28 March 2011; published 23 June 2011.

[1] We model earthquake nucleation (in 2D) on narrow faults with coupled rate-state friction and shear heating-induced thermal pressurization, including diffusive transport of heat and pore pressure. Thermal pressurization increases pore pressure p, decreasing frictional resistance. Observed fault core permeability is generally too low to mitigate thermal pressurization at subseismic slip speeds. Under drained, isothermal conditions, nucleation with the aging law is crack like, with the interior of the slip zone always near maximum slip speed. When thermal pressurization is included, it can dominate weakening at speeds of 0.02–20 mm/s for hydraulic diffusivities c_{hyd} from 10^{-8} to 10^{-3} m^2/s and nominal material parameters well before seismic radiation occurs. Dramatic along-strike localization of slip occurs due to feedback in which the area of maximum slip experiences the greatest weakening, which in turn favors more slip. With the slip law, however, nucleation is pulse like, with slip speed decaying behind the pulse tip. Thermal pressurization is diminished relative to the aging law case since most weakening occurs in locations with limited slip, yet we find that it can overwhelm frictional weakening at slip speeds in the range of 1–100 mm/s for c_{hyd} from 10^{-8} to 3×10^{-5} m^2/s. At higher slip speeds, the finite thickness of the shear zone becomes significant, reducing thermal pressurization. Even if not the dominant weakening mechanism, thermal pressurization is likely to be significant at or before the onset of seismic radiation.

Citation: Schmitt, S. V., P. Segall, and T. Matsuzawa (2011), Shear heating-induced thermal pressurization during earthquake nucleation, *J. Geophys. Res.*, *116*, B06308, doi:10.1029/2010JB008035.

1. Introduction

[2] Within the last 30 years, much attention has been directed toward the role of rock friction in the nucleation of earthquakes. According to the effective stress principle, the strength of a fault is given by $\tau = \mu(\sigma - p)$, where μ is the coefficient of friction, σ is the normal stress, and p is the pore pressure. Laboratory and theoretical work has yielded rate- and state-dependent friction laws (starting with *Dieterich* [1979]), in which μ depends on slip rate and slip history. Rate- and state-dependent friction laws have provided plausible mechanisms for earthquake nucleation that are consistent with realistic seismicity rates [*Ruina*, 1983; *Dieterich*, 1992, 1994]. At the same time, researchers [*Sibson*, 1973; *Lachenbruch*, 1980] realized that shear heating-induced thermal pressurization could lead to a loss of frictional resistance during dynamic slip for constant μ. The thermal pressurization hypothesis has subsequently been developed by many researchers [*Mase and Smith*, 1985, 1987; *Lee and Delaney*, 1987; *Andrews*, 2002; *Bizzarri and Cocco*, 2006a, 2006b; *Suzuki and Yamashita*, 2006; *Rice*, 2006], but it has been analyzed mainly in the context of fast slip. In this paper, we include thermal pressurization in numerical simulations of earthquake nucleation.

[3] The idea of shear heating-induced thermal pressurization was first proposed in the context of faulting by *Sibson* [1973], though it had earlier been proposed as a mechanism for catastrophic landslides [*Habib*, 1967]. Early work was motivated by a discrepancy between the theoretical amount of heat generated in earthquakes and the relative scarcity of geologic and geophysical evidence for such thermal signatures. The rate of frictional heat generation is proportional to the product of stress and strain rate such that, neglecting conduction, $\Delta T \propto \int \tau\dot{\gamma}\, dt$. With typical crustal normal stresses, fixed hydrostatic pore pressure, and narrow shear zones, the large strain rates in shear zones during earthquake rupture will generate sufficient heat to melt rock. Yet worldwide studies of exhumed fault zones seem not to show the expected ubiquity of friction melt pseudotachylite [e.g., *Sibson*, 1986]. Further, heat flow studies show no discernible thermal anomalies along active faults (for example, reporting on the San Andreas Fault [*Lachenbruch and Sass*, 1980]). *Sibson* [1973] addressed this discrepancy by suggesting that thermal expansion of pore fluids weakens faults during earthquake rupture such that extreme heating does not occur.

[4] In the following decades, researchers further examined the thermal pressurization hypothesis. Starting with the

[1]Department of Geophysics, Stanford University, Stanford, California, USA.
[2]National Research Institute for Earth Science and Disaster Prevention, Tsukuba, Japan.

0148-0227/11/2010JB008035

governing equations of heat, fluid flow, and dilatancy, *Lachenbruch* [1980] identified the conditions (including shear stress, strain rate, slip speed, and permeability) that allow heat and pore fluid transport to be neglected in modeling fault zone strength during slip. He found that realistic values require solving coupled equations of friction, heat, and pore pressure transport, although he analyzed only limiting cases. *Mase and Smith* [1985, 1987] performed numerical simulations of shear heating using the coupled equations with an imposed slip history and a constant friction coefficient. *Andrews* [2002] applied thermal pressurization to a propagating crack model of an earthquake source with slip-weakening friction. *Rice* [2006] compared shear fracture energies inferred from seismological observations to those predicted for a simple model of thermal pressurization with a constant friction coefficient and an imposed slip rate. Seismological estimates of fracture energy are influenced by model assumptions but independently yield values consistent with predictions of thermal pressurization, strongly suggesting that thermal pressurization is relevant to natural earthquakes. *Noda et al.* [2009] presented detailed numerical calculations including rate-state friction and thermal pressurization for artificially nucleated dynamic events, and showed that model ruptures have many characteristics in common with natural earthquakes.

[5] Despite the concurrent developments in thermal pressurization and rate- and state-dependent friction, there has been little effort to identify how they interact over an entire earthquake event from rupture nucleation to termination. Conventional wisdom has been that thermal pressurization occurs only in moderate to large earthquakes [*Kanamori and Heaton*, 2000; *Andrews*, 2002]. The origin of this notion is unclear, but it may arise from *Lachenbruch*'s [1980] statement that thermal pressurization may occur only in large earthquakes provided that fault zone permeability is near $\sim 10^{-15}$ m^2. While rock permeability varies over many orders of magnitude, recent laboratory studies of actual fault zone materials under appropriate confining pressures suggest that fault core permeabilities are much lower than this value [*Lockner et al.*, 2000; *Wibberley and Shimamoto*, 2003].

[6] Indeed, recent work suggests that thermal pressurization is significant during earthquake nucleation. *Sleep* [1995a, 1995b] realized the possibility for significant shear heating with rate and state friction in certain conditions, but did not consider the effects of fluid diffusion. *Segall and Rice* [1995] considered shear dilatancy and the resulting pore pressure effect on earthquake nucleation, and the same authors later [*Segall and Rice*, 2006] considered thermal pressurization. In the latter work, they estimate that thermal pressurization may overwhelm rate/state frictional weakening at slip speeds of 10^{-5} to 10^{-2} m/s, which are attained when an earthquake's moment release is still ten orders of magnitude smaller than those *Andrews* [2002] predicted (using a much larger value of hydraulic diffusivity, however).

[7] *Segall and Rice* [2006] present a simplified analysis to estimate when thermal pressurization is significant. They start with the slip history for an aging law nucleation zone of fixed length [*Dieterich*, 1992] and estimate the temperature rise that it would generate. Then, using hydraulic diffusivities inferred from fault cores of the Median Tectonic Line [*Wibberley and Shimamoto*, 2003] and the Nojima Fault [*Lockner et al.*, 2000], they predict the resulting pressurization rate. A critical velocity v_{crit} is defined to be when thermal pressurization dominates rate/state friction in the overall weakening. Assuming hydraulic diffusivity on the order of 10^{-6} m^2/s, *Segall and Rice* [2006] obtained a value of $v_{crit} \approx 10^{-4}$ to 10^{-3} m/s, which is well below seismic slip speeds and attained after only a modest amount of slip. Because of the coupled nature of the problem, there is feedback in which slip leads to greater shear heating, which in turn leads to greater pore fluid pressurization that enhances the weakening and allows for even more slip. The analysis of *Segall and Rice* [2006] neglects this feedback and also simplifies the elastic interaction of an evolving nucleation zone by assuming a fixed nucleation zone size.

[8] Our present work builds upon the analysis of *Segall and Rice* [2006]. Using numerical models of predominantly zero-width faults embedded in a 2D diffusive domain, we explore the behavior of the coupled system of rate- and state-dependent friction, shear heating-induced thermal pressurization, and pore pressure diffusion. By solving the system numerically in an elastic diffusive continuum, we include the thermal weakening feedback process and allow the nucleation zone to evolve in size. The main goal of this work is to identify when thermal pressurization dominates fault weakening, which will ultimately influence the initial conditions of dynamic ruptures.

2. Model and Mathematical Description

2.1. Model Geometry and Physical Basis

[9] The fault model is motivated by recent observations of fault zones in which slip appears to be hosted within a narrow, low-permeability fault core (Figure 1a). That conceptual model is based on studies of two Japanese faults and two Southern California faults. *Wibberley and Shimamoto* [2003] measured the permeability of fault core material from the Median Tectonic Line (MTL) in Japan, and found a low permeability ($\sim 10^{-19}$ m^2 at 80–180 MPa confining pressure) fault core of width ~0.1 m surrounded by a higher-permeability ($\sim 10^{-16}$ to $\sim 10^{-14}$ m^2) damage zone. *Lockner et al.* [2000] measured the permeability of drill core samples from 1500 m depth on the Nojima fault. They found similar properties at 50 MPa confining pressure: a narrow fault core with permeability of $\sim 10^{-19}$ to $\sim 10^{-18}$ m^2 and a surrounding damage zone with permeability of $\sim 10^{-17}$ to $\sim 10^{-16}$ m^2.

[10] The width of the actively shearing zone is a key parameter in the analysis of thermal pressurization. Geologists have undertaken several field studies to quantify the thickness of shear zones active during seismic slip (summarized by *Sibson* [2003]). Shear zone thicknesses of 1–10 mm have been observed in slickenside material, pseudotachylites, and intravein septa in laminated quartz veins (thin layers of wall rock thought to be remnants of slip on the vein margin). Gouge shear zones appear to be wider, with thicknesses of 3–300 mm. The distribution of shear strain inside shear zones is not as well documented. Thin section analysis of samples from the North Branch San Gabriel fault [*Chester et al.*, 1993] and the Punchbowl fault [*Chester and Chester*, 1998] suggest that extreme shear localization may occur during earthquakes. These authors document a 0.6–1.1 mm apparent shear zone, within which most slip occurs in a zone of width 100–300 μm [*Rice*, 2006]. No

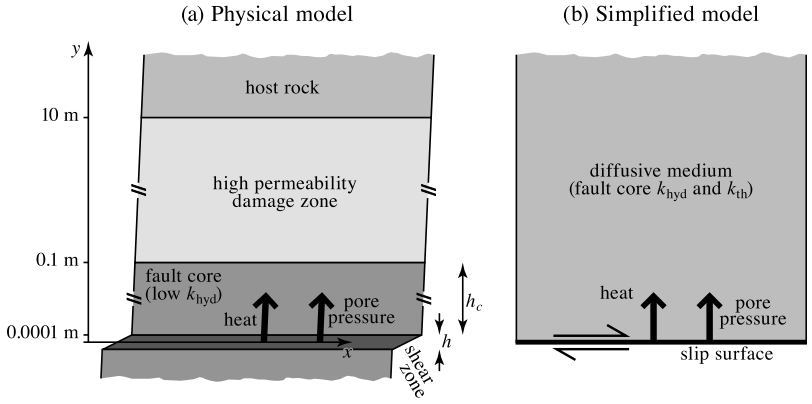

Figure 1. (a) The fault zone model motivated by field and drill core observations. A narrow principal shear zone is surrounded by a low-permeability fault core. Further away from the shear zone is a high-permeability damage zone. Distances in the y direction (away from the shear zone) are indicated to the left; the figure is not drawn to scale. (b) Simplified fault zone model used in this work. In this paper, we generally neglect the shear zone thickness and treat it as slip on a surface. The thermal boundary layer that develops during the times considered in this paper is smaller than the fault core, so we model transport only in a diffusive medium with the properties of the fault core.

signatures of extreme shear localization were documented in the MTL sample, but *Rice* [2006] reports that the researchers observed a <3 mm central slip zone believed to be from the most recent earthquake.

[11] We model the fault core and slip zone in a simplified manner (Figure 1). First, we replace the heterogeneous permeability distribution of Figure 1a with a homogeneous medium of low permeability, as shown in Figure 1b. This simplification is justified if the diffusion time across the low permeability fault core (of width h_c) is much greater than the duration of significant frictional heating during earthquake nucleation. The characteristic diffusion time is

$$t_{\text{diff}} = \frac{h_c^2}{4c} \ , \tag{1}$$

where c is diffusivity (here, the larger of thermal or hydraulic diffusivities). The remaining nucleation time is

$$t - t_{\text{inst}} \approx C\frac{d_c}{v(t)} \ , \tag{2}$$

where C is a constant of order unity and d_c is the characteristic slip distance of frictional state evolution. Setting $t_{\text{diff}} = t - t_{\text{inst}}$ reveals that fault cores of width $h_c \gtrsim \sqrt{4cd_c/v}$ are effectively infinite on timescales of earthquake nucleation. For fault core diffusivity 10^{-6} m^2/s, d_c = 100 μm, and $v_i = 10^{-6}$ m/s (well below speeds where thermal pressurization becomes significant), we find $h_c \approx 0.02$ m. *Sibson* [2003] indicates that 0.1 m is a typical width of the fault core, but in some cases it may be as narrow as 0.01 m. For many faults, however, the transient boundary layer that develops during nucleation is likely to be smaller than the width of the fault core, and in that circumstance we may neglect the material heterogeneity farther from the fault.

[12] Our second simplification is that, in most of our analysis, we treat the shear zone as a zero-thickness slip surface instead of a zone with finite width. Such an approximation is valid for times that are long compared to the characteristic diffusion time across the shear zone. Employing the same relations of equations (1) and (2), but replacing h_c with the shear zone half width $h/2$ and solving for the limiting slip speed v, we find

$$v \lesssim \frac{16cd_c}{h^2} \ . \tag{3}$$

For example, if the width of the shear zone is h = 200 μm, the larger diffusivity is $c = 10^{-6}$ m^2/s, and d_c = 50 μm, then the limiting slip speed is 0.02 m/s. For lower slip speeds, neglect of the finite shear zone width is reasonable. We explore this question further in section 6.3.

[13] We treat diffusion of heat and pore pressure only in the fault-normal direction; this simplification is justified because the thermal boundary layer that arises from shear heating is on the order of 10^{-2} m (assuming 100 s of significant heat generation at the boundary of a medium with diffusivity 10^{-6} m^2/s), while the distribution of heat sources along the fault vary according to the length scale of rate/state frictional nucleation zones, which are on the order of several meters for the parameters used in this study. Tests including 2D diffusion confirm the validity of this approximation. We further simplify by ignoring advection of heat by the pore fluid; this effect is negligible because both pore volume and fluid velocity are small [*Lee and Delaney*, 1987; *Vredevoogd et al.*, 2007].

2.2. Governing Equations

2.2.1. Rate- and State-Dependent Friction

[14] Consistent with numerous studies on earthquake nucleation, we use rate- and state-dependent friction, which is so named because it depends on slip rate and history (state). The constitutive relation is [*Ruina*, 1983]

$$\tau_{\text{fric}} = \mu\sigma_{\text{eff}} = \left[\mu_0 + a\ln\frac{v}{v_0} + b\ln\frac{\theta v_0}{d_c}\right]\sigma_{\text{eff}} \ , \tag{4}$$

which relates shear strength τ_{fric} to effective normal stress $\sigma_{\text{eff}} = (\sigma - p)$ through a friction coefficient μ. The friction coefficient μ depends on slip rate v and state θ, which has dimension of time and evolves over characteristic distance d_c. The parameters a and b are dimensionless material constants on the order of 0.01. We analyze the two forms of state evolution law in common use: one referred to as the "aging law," and the other referred to as the "slip law." They are [*Ruina*, 1983]

$$\frac{d\theta}{dt} = 1 - \frac{\theta v}{d_c} , \qquad \text{the aging law, and} \tag{5}$$

$$\frac{d\theta}{dt} = -\frac{\theta v}{d_c} \ln \frac{\theta v}{d_c} , \qquad \text{the slip law.} \tag{6}$$

For both laws, the steady state value is $\theta_{ss} = d_c/v$, but the two state evolution laws yield different behavior in response to an abrupt change in sliding velocity. Following a step increase in velocity, the aging law predicts evolution of friction toward steady state over a slip distance proportional to the velocity change, while slip law friction predicts a characteristic evolution distance that is independent of the velocity change. *Ampuero and Rubin* [2008] demonstrated that, under drained, isothermal conditions (fixed σ_{eff}), the two state evolution laws yield profoundly different nucleation behaviors. They found that aging law nucleation takes the form of a quasi-statically growing crack for $0.5 \lessapprox a/b < 1$ or a fixed length slip zone for $a/b < 0.5$, while slip law nucleation is more pulse like. Laboratory velocity-stepping experiments tend to exhibit behavior more consistent with the slip law [*Nakatani*, 2001]; for that reason *Ampuero and Rubin* [2008] favor the slip law in the context of frictional nucleation. Laboratory experiments with surfaces in stationary contact, however, favor the aging law [*Dieterich and Kilgore*, 1994].

[15] *Linker and Dieterich* [1992] found that variable effective normal stress $\sigma_{\text{eff}}(t)$ also affects the coefficient of friction μ. This effect is relevant to the present work because effective stress varies due to the thermal pressurization. *Linker and Dieterich* [1992] defined a constitutive relationship in which the variable normal stress affects the frictional state,

$$\frac{d\theta}{dt} = \begin{bmatrix} \text{state evolution} \\ \text{law(5)or(6)} \end{bmatrix} - \frac{\alpha\theta}{b\sigma_{\text{eff}}} \frac{d\sigma_{\text{eff}}}{dt} , \tag{7}$$

where α is a coefficient in the range of 0 to μ_0. For $\alpha = 0$, the normal stress effect vanishes; that is, a step change in σ_{eff} results in an instantaneous change of τ to its new value. Increasing α decreases the instantaneous response. With $\alpha = \mu_0$, a step change in σ_{eff} results in a gradual evolution toward the final value of τ with no instantaneous change. *Linker and Dieterich* [1992] and *Richardson and Marone* [1999] find values of $\alpha \approx 0.3$ agree with laboratory experiments.

2.2.2. Thermal Transport

[16] For spatially uniform properties, the equation for thermal diffusion with a shear heating source (neglecting diffusion parallel to the fault) is

$$\tau \frac{d\gamma}{dt} + k_{\text{th}} \frac{\partial^2 T}{\partial y^2} = \rho c_v \frac{\partial T}{\partial t} , \tag{8}$$

where γ is shear strain, ρ is the bulk density of the rock and pore fluid, k_{th} is thermal conductivity, and c_v is heat capacity (a typical value of ρc_v is 2.8 MPa/K). Outside of the shear zone we neglect shear heating, so equation (8) reduces to homogeneous diffusion equation

$$\frac{\partial T}{\partial t} = c_{\text{th}} \frac{\partial^2 T}{\partial y^2} \quad \text{for} \quad y > 0 , \tag{9}$$

where $c_{\text{th}} = k_{\text{th}}/\rho c_v$ is the thermal diffusivity. Typical values of c_{th} are very near 10^{-6} m^2/s [*Rice*, 2006]. For heat generation and transport within the shear zone, we consider energy conservation over a finite width shear zone extending from $y = -h$ to $y = 0$:

$$\tau\left(h\frac{d\gamma}{dt}\right) + 2k_{\text{th}} \left.\frac{\partial T}{\partial y}\right|_{y=0} - \rho c_v h \frac{\partial T}{\partial t} = 0 \quad \text{for} \quad -h < y < 0 , \tag{10}$$

where the first term is shear heating, the second term is heat flux out of the two sides of the shear zone, and the third term is the increase in thermal energy inside the shear zone. For times much longer than the characteristic diffusion time across the shear zone (that is, $\Delta t \gg h^2/c_{\text{th}}$), we may make the approximation $h \approx 0$. Under that circumstance, the heat storage vanishes so we can rewrite equation (10) as a Neumann boundary condition on the diffusion domain,

$$\left.\frac{\partial T}{\partial y}\right|_{y=0} = -\frac{\tau v}{2\rho c_v c_{\text{th}}} , \tag{11}$$

where $v = \int_{-h}^{0} \dot{\gamma}\, dy$. We call this the "zero-width shear zone approximation," and we use it extensively throughout this paper.

2.2.3. Fluid Transport

[17] Our model fault zone consists of a low-permeability fault core that flanks the shear zone. Beyond the fault core is a much more permeable damage zone that effectively remains at ambient pore pressure p_0. *Segall and Rice* [2006] derive the pore pressure source and transport equations in detail; we summarize them here. Inside the wall zone (but outside the shear zone), pore pressure satisfies

$$\frac{\partial p}{\partial t} = c_{\text{hyd}} \frac{\partial^2 p}{\partial y^2} + \Lambda \frac{\partial T}{\partial t} . \tag{12}$$

Typical values of hydraulic diffusivity are within a few orders of magnitude of $c_{\text{hyd}} \approx 10^{-6}$ m^2/s. The hydraulic diffusivity is related to hydraulic permeability k_{hyd} via the relationship

$$c_{\text{hyd}} = \frac{k_{\text{hyd}}}{\beta_{\text{eff}}\eta} , \quad \text{where } \beta_{\text{eff}} = \phi\left(\beta_f + \beta_\phi\right) . \tag{13}$$

In equation (13), η is the pore fluid viscosity, β_f is the pore fluid compressibility, ϕ is the porosity, and β_ϕ is the pore compressibility. The source term in equation (12) is the thermal pressurization; the coefficient of thermal pressurization Λ is the ratio of the difference of pore and pore fluid thermal expansivity $(\lambda_f - \lambda_\phi)$ to the compressibility of the pore fluid and the pores,

$$\Lambda = \frac{\phi\left(\lambda_f - \lambda_\phi\right)}{\beta_{\text{eff}}} . \tag{14}$$

Table 1. Notation

Symbol	Quantity	Nominal Value or Reference
μ_0	nominal value of friction	0.6
a	velocity dependence of friction	0.012
b	state dependence of friction	0.015
α	dependence of θ on $\dot{\sigma}_{\text{eff}}$	0 to 0.6
d_c	characteristic frictional slip weakening distance	10^{-4} m
G	shear modulus	10 GPa
v_s	shear wave speed, for radiation damping	3700 m/s
c_{th}	thermal diffusivity	10^{-6} m^2/s
c_{hyd}	pore pressure diffusivity	10^{-6} m^2/s
Λ	thermal pressurization factor	0.8 MPa/K
ρc_v	volumetric heat capacity	2.86 MPa/K
$\sigma - p_0$	background effective stress	140 MPa
$\dot{\tau}_\infty$	stressing rate	0.01 Pa/s
v_0	friction reference velocity	Equation (4)
L_{min}	minimum half length for unstable nucleation zone	Equation (25)
L_∞	maximum aging law nucleation zone half length	Equation (35)
h	shear zone thickness	Sections 2.1 and 6.3
μ	friction coefficient	Equation (4)
v	slip velocity	Equation (20)
θ	frictional state	Equation (5) and (6)
$v_{\text{max}}(t)$	maximum sliding velocity at time t	
v_{crit}	v_{max} when $\lvert\mu_0\dot{p}\rvert > \lvert\dot{\mu}(\sigma - p_0)\rvert$	Equation (37)
T	temperature	Equations (9) and (11)
p	pore pressure	Equations (12) and (16)
σ_{eff}	effective normal stress $\sigma - p_0 - p$	
t_{nst}	time of the earthquake	Sections 3.1, 4.1, and 4.2

Reasonable values of Λ fall in the range 0.6–1.1 MPa/K [*Segall and Rice*, 2006]. Inside the shear zone, fluid mass conservation requires

$$\frac{\partial p}{\partial t} = \Lambda \frac{\partial T}{\partial t} - \frac{2c_{\text{hyd}}}{h} \left.\frac{\partial p}{\partial y}\right|_{y=0} . \tag{15}$$

In the case of the zero-width shear zone, $\partial p/\partial y|_{y=0} = 0$. For a homogeneous medium with diffusion perpendicular to a zero-width fault, *Rice* [2006, Appendix B4] found that pore pressure on the fault (that is, at $y = 0$) is directly related to the temperature rise through the relationship

$$\Delta p(y=0) = \frac{\Lambda}{1 + \sqrt{c_{\text{hyd}}/c_{\text{th}}}} \Delta T(y=0) . \tag{16}$$

We leverage this relationship to yield a significant reduction in computational expense, since in the limit $h \to 0$ it allows us to simulate numerically the temperature field while directly computing $\Delta p(y = 0)$, rather than simultaneously computing thermal and pore pressure diffusion.

2.2.4. Stress Interaction, Seismic Radiation, and Governing Equation for Slip

[18] In modeling earthquake nucleation in a continuum, we must calculate the elastic stress that arises from slip on the fault. For a 1D fault in a 2D continuum, the stress interaction is computed as a Hilbert transform of the displacement gradient. For antiplane deformation,

$$\tau_{\text{el}}(x) = \tau_\infty - \frac{G}{2\pi} \int_{-\infty}^{\infty} \frac{1}{x - \xi} \frac{\partial \delta}{\partial \xi} \, d\xi , \tag{17}$$

where τ_∞ is the remote (tectonic) stress. For plane strain deformation in equation (17), G is replaced by $G/(1 - \nu)$, where ν is Poisson ratio. The Fourier transform of (17) can be written as

$$\hat{\tau}_{\text{el}}(m) = \hat{\tau}_\infty - \hat{k}(m)\, \hat{\delta} , \tag{18}$$

where $\hat{k}(m)$ is an effective stiffness that depends on spatial wave number m (for antiplane deformation, $k = G|m|/2$) [e.g., *Segall*, 2010]. Determining the elastic stress interaction in the Fourier domain using an FFT is computationally efficient.

[19] As slip speeds grow to within a few orders of magnitude of elastic wave speeds, inertial effects become important. Because our focus is on nucleation, we employ the "radiation damping" approximation [*Rice*, 1993] rather than full elastodynamics [e.g., *Lapusta et al.*, 2000]. Radiation damping is given by

$$\tau_{\text{rad}} = \frac{G}{2v_s} v , \tag{19}$$

which gives the stress change due to radiation of plane s waves.

[20] With equations for elasticity (17), friction (4), and radiation (19), we write the governing equation for the fault slip as $\tau_{\text{el}} - \tau_{\text{fric}} - \tau_{\text{rad}} = 0$, which expands to

$$\tau_\infty - \frac{G}{2\pi} \int_{-\infty}^{\infty} \frac{1}{x - \xi} \frac{\partial \delta}{\partial \xi} \, d\xi - \left(\mu_0 + a \ln \frac{v}{v_0} + b \ln \frac{\theta v_0}{d_c}\right) [\sigma - p(t)] - \frac{G}{2v_s} v = 0 . \tag{20}$$

The effects of thermal pressurization act through the pore pressure term in τ_{fric}. The weakening rates due to friction and thermal pressurization become separate terms in the time derivative of the force balance (20), which is

$$\dot{\tau}_\infty - \frac{G}{2\pi} \int_{-\infty}^{\infty} \frac{1}{x - \xi} \frac{\partial v}{\partial \xi} \, d\xi - [\sigma - p(t)] \left(\frac{a}{v}\frac{dv}{dt} + \frac{b}{\theta}\frac{d\theta}{dt}\right) + \left(\mu_0 + a \ln \frac{v}{v_0} + b \ln \frac{\theta v_0}{d_c}\right) \frac{dp}{dt} - \frac{G}{2v_s}\frac{dv}{dt} = 0 . \tag{21}$$

In this study, we assume parameters consistent with a depth of 7 km; their nominal values are in Table 1. Hydraulic properties are motivated by the observations from Japan [*Lockner et al.*, 2000; *Wibberley and Shimamoto*, 2003]. The frictional parameter $(b - a)$ is consistent with the observations of *Blanpied et al.* [1995], while the value of d_c is set at the high end of laboratory observations at 100 μm. This value of d_c does favor thermal pressurization relative to $d_c \sim 10$ μm, though we explore the dependence on d_c in sections 2.3 and 5.4.

[21] To estimate when radiation damping becomes important, we estimate the velocity at which it balances the velocity dependence of rate/state friction in isothermal nucleation. Momentarily neglecting thermal pressurization, we rearrange equation (21) to obtain

$$\left(\frac{a}{v} + \frac{G}{2\sigma_{\text{eff}} v_s}\right) \frac{dv}{dt} = \frac{1}{\sigma_{\text{eff}}} \frac{d\tau_{\text{el}}}{dt} - \frac{b}{\theta}\frac{d\theta}{dt} . \tag{22}$$

From this it is apparent that radiation damping dominates at speeds $v > 2av_s\sigma_{\text{eff}}/G$, which is about 0.9 m/s for the nominal values shown in Table 1. To identify conditions for which the quasi-dynamic governing equation is valid, *Rice et al.* [2001] show that for slip speeds

$$v \ll 2\sqrt{a(b-a)}\frac{\sigma_{\text{eff}}v_s}{G} \ , \tag{23}$$

solutions are effectively equivalent to those of the elastodynamic equations. For our nominal values of system parameters, quasi-dynamic analysis is sufficient for $v \ll 0.5$ m/s. The speed at which radiation damping and elastodynamic effects become important is proportional to the effective normal stress. The effective normal stress is not well known at seismogenic depths. For hydrostatic pore pressures, neglecting inertial terms is reasonable for $v \lessapprox 0.1$ m/s, but both the radiation damping term and wave-mediated effects would be significant at much lower slip speeds for near-lithostatic pore pressure.

2.3. Dimensional Analysis

[22] Writing the governing equations in a nondimensional form gives insight into the effects of the various system parameters. We define a nondimensional frictional strength as

$$\hat{\tau} = \frac{\tau_{\text{fric}}}{\mu_0(\sigma - p_0)} \ ,$$

where p_0 is the background pore pressure. In our simulations, we apply a constant remote stressing rate $\dot{\tau}_\infty$, which can be related to a velocity through the nucleation zone stiffness k. In the spring-slider analogue, linear stability analysis [*Ruina*, 1983] reveals that small perturbations become unstable if the spring's stiffness is less than a critical value given by

$$k_{\text{crit}} = \frac{\sigma_{\text{eff}}(b-a)}{d_c} \ . \tag{24}$$

In an elastic continuum the stiffness is directly proportional to the elastic modulus and inversely proportional to the half length of the sliding zone, or $k \approx G/2L$. Hence we can define a characteristic length

$$L_{\text{min}} = \frac{Gd_c}{2(b-a)(\sigma - p_0)} \ , \tag{25}$$

which is the minimum half length of a nucleation zone capable of accelerating to instability [e.g., *Rubin and Ampuero*, 2005]. We then obtain the nondimensional along-fault coordinate

$$\hat{x} = \frac{x}{L_{\text{min}}} = \frac{2(b-a)(\sigma - p_0)x}{Gd_c} \ . \tag{26}$$

A characteristic velocity can be defined based on the imposed stressing rate $\dot{\tau}_\infty$:

$$v_\infty = \frac{\dot{\tau}_\infty}{k_{\text{crit}}} = \frac{d_c}{(b-a)(\sigma - p_0)}\dot{\tau}_\infty \ . \tag{27}$$

The velocity v_∞ represents the slip speed in a hypothetical locked zone with stiffness k_{crit} that experiences stress rate $\dot{\tau}_\infty$. Slip speed, time, and frictional state thus have sensible normalizations given by

$$\hat{v} = \frac{v}{v_\infty} \ , \quad \hat{t} = \frac{tv_\infty}{d_c} \ , \quad \text{and} \quad \hat{\theta} = \frac{\theta v_\infty}{d_c} \ .$$

For a homogeneous medium there is no characteristic distance for heat and pore fluid transport away from the fault, so we define one to be the pore pressure diffusion length corresponding to time d_c/v_∞. Thus, nondimensional distance perpendicular to the fault is

$$\hat{y} = y\sqrt{\frac{v_\infty}{c_{\text{hyd}}d_c}} \ .$$

We define nondimensional temperature and pore pressure changes by

$$\hat{T} = \frac{T\Lambda}{\sigma - p_0} \quad \text{and} \quad \hat{p} = \frac{p}{\sigma - p_0} \ .$$

The nondimensional rate- and state-dependent frictional resistance (4) becomes

$$\hat{\tau} = \left(1 + \frac{a}{\mu_0}\log\hat{v} + \frac{b}{\mu_0}\log\hat{\theta}\right)(1 - \hat{p}) \ , \tag{28}$$

with state evolution laws (from 5–7)

$$\frac{d\hat{\theta}}{d\hat{t}} = \begin{cases} 1 - \hat{\theta}\hat{v} + \dfrac{\alpha\hat{\theta}}{b(1-\hat{p})}\dfrac{d\hat{p}}{d\hat{t}} \ , & \text{the aging law, or} \\ -\hat{\theta}\hat{v}\log\left(\hat{\theta}\hat{v}\right) + \dfrac{\alpha\hat{\theta}}{b(1-\hat{p})}\dfrac{d\hat{p}}{d\hat{t}} \ , & \text{the slip law.} \end{cases} \tag{29}$$

The pore pressure diffusion equation (12) simplifies to

$$\frac{\partial\hat{p}}{\partial\hat{t}} = \frac{\partial^2\hat{p}}{\partial\hat{y}^2} + \frac{\partial\hat{T}}{\partial\hat{t}} \ , \tag{30}$$

while the thermal diffusion equation (9) transforms to

$$\frac{\partial\hat{T}}{\partial\hat{t}} = \mathcal{D}\frac{\partial^2\hat{T}}{\partial\hat{y}^2} \ , \tag{31}$$

with $\mathcal{D} = c_{\text{th}}/c_{\text{hyd}}$. The Neumann boundary condition (11) becomes

$$\left.\frac{\partial\hat{T}}{\partial\hat{y}}\right|_{\hat{y}=0} = -\frac{\mu_0\Lambda}{2\rho c_v}\sqrt{\frac{v_\infty d_c}{c_{\text{th}}}}\sqrt{\frac{c_{\text{hyd}}}{c_{\text{th}}}}\hat{\tau}\hat{v} = -\mathcal{F}\mathcal{D}^{-1/2}\hat{\tau}\hat{v} \ , \tag{32}$$

where the nondimensional group $\mathcal{F}\mathcal{D}^{-1/2}$ quantifies the intensity of thermal pressurization. This group is equivalent to the "thermal pressurization efficiency" E_T of *Segall et al.* [2010]. In terms of stressing rate,

$$\mathcal{F} = \frac{\mu_0\Lambda}{2\rho c_v}\sqrt{\frac{v_\infty d_c}{c_{\text{th}}}} = \frac{\mu_0 d_c\Lambda}{2\rho c_v}\sqrt{\frac{\dot{\tau}}{c_{\text{th}}(b-a)(\sigma - p_0)}} \ .$$

The zero-width shear zone p-T relationship of equation (16) simplifies to

$$\hat{p}(\hat{y}=0) = \frac{\hat{T}(\hat{y}=0)}{1+\mathcal{D}^{-1/2}} . \quad (33)$$

We thus identify five nondimensional groups in equations (28)–(33): a/μ_0, a/b, α/μ_0, $\mathcal{D}$ and $\mathcal{F}$. The first two nondimensional groups are the well documented [e.g., *Ampuero and Rubin*, 2008] parameters governing rate- and state-dependent frictional nucleation. The nondimensional group α/μ_0 is from the *Linker and Dieterich* [1992] constitutive law; in this case it controls how quickly friction responds to a change in pore pressure. In some studies (for example, slip on a bimaterial fault [*Cochard and Rice*, 2000]) this effect has important physical implications. In the present study, the effect is crucial for numerical well posedness (see Section 3.4), but does little to affect the overall behavior of the system.

[23] The diffusivity ratio $\mathcal{D}$ measures relative rates of heat and pore fluid diffusion, and is the least well constrained of the parameters, due to uncertainty in permeability. Both thermal and fluid diffusion diminish shear heating-induced thermal pressurization. With $c_{hyd} \ll c_{th}$, thermal conduction dominates diffusion away from the fault, while for $c_{hyd} \gg c_{ut}$ pore fluid diffusion is the primary diffusive mechanism. Since c_{hyd} is the least well known of all of the material properties relevant to thermal pressurization, we study its effect in detail (section 5.5).

[24] The remaining nondimensional group $\mathcal{F}$ is a measure of shear heating source strength: larger values of ρc_v (volumetric heat capacity) or c_{th} diminish the temperature rise, while stronger system loading via v_∞ or longer slip weakening distances d_c will enhance shear heating. The thermal pressurization factor Λ enters $\mathcal{F}$ because of the scaling of temperature on the fault with pore pressure.

[25] There are two additional nondimensional groups not analyzed in detail here. Since this study focuses on the zero shear zone width approximation, the ratio h/d_c does not appear. Some laboratory work has been done to estimate h/d_c; for example, *Marone and Kilgore* [1993] propose $h = 100d_c$. A limited number of finite shear zone width calculations are described in section 6. Another nondimensional group is W/L_{min}, where W is the along-strike dimension of the fault. For slip events that become large enough that the fault length is important, or for which the nucleation dimension is a significant fraction of W, the ratio W/L_{min} can be critical in controlling the behavior (for example, the slow slip events of *Liu and Rice* [2005] or *Segall* [2010]). In the present work the fault length is large compared to the nucleation dimension, $W \gg L_{min}$, which we expect to be the norm for earthquakes.

2.4. Numerical Implementation

[26] Using the zero-width shear zone approximation, we couple a 2D finite difference code with a boundary integral elasticity formulation to simulate nucleation with thermal pressurization. With the time derivative of the stress balance, equation (21), we can pose the problem in the form of a system of coupled ODEs. We integrate v, θ, and T using an explicit Runge-Kutta method (see Appendix A). For the short integration times considered here, this approach introduces negligible error.

[27] The fault is modeled as one edge of a finite difference grid used to calculate thermal diffusion. We impose the Neumann boundary condition (11) at the fault, which introduces the appropriate shear heating at $y = 0$. With a zero-width shear zone and homogeneous material properties, pore pressure may be obtained directly from the computed temperature using equation (16). We calculate the elastic stress interaction in the Fourier domain using equation (18).

[28] The finite difference grid adaptively remeshes as accuracy demands. Early in nucleation, temperature gradients are slight, yet over long time intervals the temperature perturbation extends far from the fault. As slip accelerates, however, the heat generation progressively outweighs thermal diffusion. Hence the largest temperature gradients occur near the fault, and solution accuracy is limited by our ability to correctly discretize those steep gradients. Therefore, when accuracy requires smaller grid point spacing away from the fault, we halve the grid spacing in the y dimension. In order to yield acceptable numerical accuracy, our simulations take explicit time steps limited by the Courant-Friedrichs-Lewy (CFL) condition, $\Delta t \leq \Delta y^2/2c_{th}$, though the ODE solver method's automatic time step selections are usually more conservative.

[29] The system is driven by a constant remote stressing $\dot{\tau}_\infty = 0.01$ Pa/s (0.3 MPa/yr). We initiate simulations with all points on the fault sliding at tectonic velocities randomly distributed near 10^{-9} m/s and below steady state (that is, $v\theta/d_c < 1$). These initial conditions cause deceleration of slip until sufficient stress accumulates to drive the fault back toward steady state. Thermal pressurization during this phase is negligible; we therefore avoid the computational expense of diffusion by integrating only isothermal rate- and state-dependent friction until the initial formation of a nucleation zone. Tests have shown that we may use this simplification without any detectable influence on the much later phase of the simulations when thermal pressurization becomes significant.

3. Results: Aging Law Nucleation

3.1. Comparison to Isothermal, Drained Nucleation

[30] One of our main goals of this work is to examine how nucleation is affected by thermal pressurization. Before performing such a comparison, we summarize some characteristics of isothermal, drained nucleation. For both forms of the state evolution law, the initial stage of nucleation is localization of slip in a zone of half length L_{min}, starting at speeds that will be on the order of v_∞. We shall call this the "initial weakening phase." After some amount of slip occurs in the initial weakening phase, nucleation behavior transitions to a different mode. *Rubin and Ampuero* [2005] found that for $a/b \lessapprox 0.5$, acceleration proceeded on a fixed length zone of dimension

$$L_\nu \approx 1.38 \frac{Gd_c}{b\sigma_{eff}} . \quad (34)$$

For $0.5 \lesssim a/b < 1$, *Rubin and Ampuero* [2005] found that nucleation takes the form of a growing crack. That is, the nucleation zone grows wider as it accelerates, and the

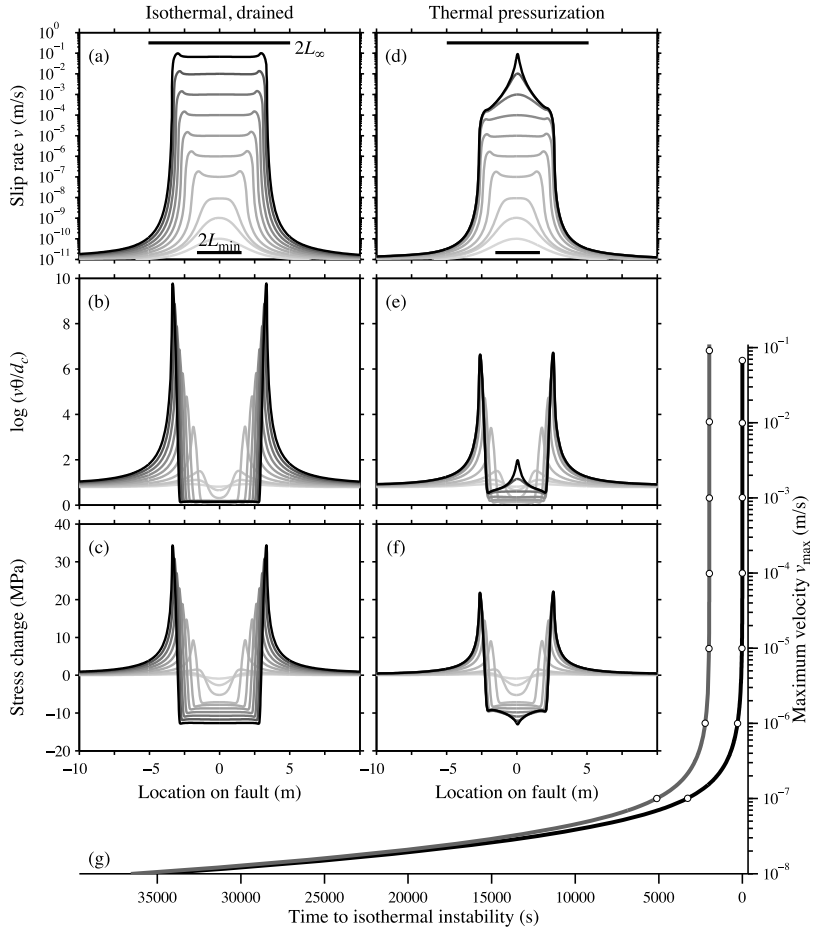

Figure 2. Comparison of aging law nucleation (a-c) without and (d-f) with thermal pressurization. Snapshots of parameters on the fault are shown. The time interval between snapshots is not uniform; rather, snapshots are taken at every decade in slip speed in the middle of the nucleation zone. Figures 2a and 2d show snapshots of slip speed on the fault. The qualitative difference above 10^{-4} m/s suggests when thermal pressurization begins to dominate fault weakening inside the nucleation zone. Bars of width $2L_{min}$ (bottom) and $2L_\infty$ (top) are shown. Figures 2b and 2e are snapshots of $\log_{10}(v\theta/d_c)$, which is a measure of how far the fault is from frictional steady state. In isothermal, drained nucleation (Figure 2b), the interior of the nucleation zone is slightly above steady state in these simulations. With thermal pressurization (Figure 2e), the interior of the nucleation zone is driven above steady state when thermal pressurization dominates. Figures 2c and 2f are snapshots of frictional resistance to slip. In isothermal, drained aging law nucleation (Figure 2c), the stress drop inside the nucleation zone is nearly uniform. With thermal pressurization (Figure 2f), the stress drop is not uniform inside the nucleation zone. Figure 2g shows slip speed in the middle of the nucleation zone over time with and without thermal pressurization. Thermal pressurization only slightly advances the time of the instability. Dots correlate to the snapshots shown in Figures 2a–2f.

interior of the crack continues to slip. Using fracture mechanics arguments, they show that the half width asymptotically approaches

$$L_\infty = \frac{G\, d_c\, b}{\pi (b-a)^2 \sigma_{\text{eff}}} \quad . \tag{35}$$

We assume typical laboratory-inferred values of a and b with $a/b = 0.8$, which correspond to the crack-like nucleation regime. Isothermal, drained simulations (shown Figure 2, left) agree with the results of *Rubin and Ampuero* [2005]. After slip of ~$10d_c$ (an amount that depends on $\dot{\tau}_\infty$ and the initial conditions), the nucleation zone transitions from the initial slip-weakening phase to a growing crack approaching width $2L_\infty$. Inside the nucleation zone, slip is nearly at steady state, which can be seen in plots of $\log(v\theta/d_c)$ in Figure 2b. As the nucleation zone accelerates, steady state velocity weakening scales with ln v, which is shown by the regularly spaced snapshots of stress drop inside the nucleation zone in Figure 2c. This is understood by noting that at steady state, ln $(v\theta/d_c) = 0$ and $\mu(v, t) = \mu_0 + (a - b)\ \ln[v(t)/v_0]$.

[31] With shear heating-induced thermal pressurization included, aging law nucleation is markedly different (right column of Figure 2). In these simulations, we use typical

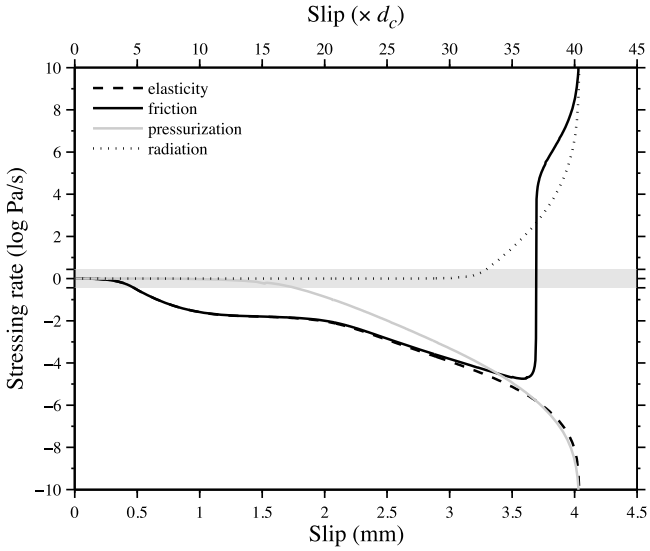

Figure 3. Terms in the stress rate equation (21) at the center of the nucleation zone, plotted against cumulative slip at that location. Negative values indicate weakening. The vertical scale is logarithmic in both directions away from the horizontal axis (in the shaded area, values between $-e$ and e are on a linear scale).

values of the friction and diffusion parameters (though d_c is somewhat large at 100 μm), but we exclude the effect of variable normal stress on frictional state (that is, $\alpha = 0$). At low slip speeds (compare the snapshots of slip speed in plots [a] and [d]), the two cases are identical. As the maximum slip speed increases, however, nucleation becomes qualitatively different. In those snapshots, slip speed ceases to be nearly uniform in the middle of the nucleation zone; rather, it localizes along strike. The qualitative deviation from isothermal, drained nucleation indicates a critical velocity v_{crit} above which thermal pressurization dominates the weakening of the fault. At even higher slip speeds, the localization of slip is dramatic. If allowed to progress without radiation damping, we find that the nucleation zone length eventually tends toward zero, regardless of the numerical discretization along the fault. This singularity in nucleation zone dimension indicates that the physical problem is poorly posed, which we consider further in section 3.3.

[32] Figures 2b and 2e compare the frictional state in the two cases. As mentioned above, the interior of the nucleation zone in the isothermal, drained case is very near steady state. With thermal pressurization, the interior of the nucleation zone is driven above steady state when $v > v_{crit}$. There, direct velocity strengthening (the a term) in rate/state friction determines the frictional response.

[33] Figures 2c and 2f compare the frictional resistance to slip τ_{fric} in the two cases. With thermal pressurization, the stress drop inside the nucleation zone is not uniform. The feedback inherent in thermal pressurization is apparent in the localization of the stress drop corresponding to the localization of slip. While difficult to see in Figure 2f, there is also a small amount of healing (an increase in τ_{fric}) that occurs on the flanks of the localized slipping zone.

[34] Thermal pressurization weakens the fault more than rate-and-state friction alone, so we expect that it will advance the time of the frictional instability t_{inst}. Our simulations confirm that prediction, as shown in Figure 2g. The time advance is modest; in the simulations of Figure 2, the advance of the instability is 8×10^2 s ahead of the 8×10^8 s between the start of the simulation and the frictional instability in the isothermal case.

[35] Since maximum slip and slip speed are colocated at the middle of the nucleation zone in aging law nucleation (with or without thermal pressurization), it is instructive to examine the contributions to the stress rate (equation (21)) there in order to understand how thermal pressurization affects the frictional resistance. In Figure 3, we track their evolution with slip. For slip of less than ~$20d_c$ (2 mm), rate/state friction is the only significant weakening mechanism, and it is entirely balanced by elasticity. As slip proceeds over the next ~$14d_c$ (1.4 mm), rate/state friction continues to dominate the fault weakening, but thermal pressurization increases in magnitude until it eventually becomes dominant. The crossover when $|\mu_0\dot{p}| > |\sigma_{eff}\dot{\mu}|$ defines v_{crit}, which we examine in more detail in section 3.2. With thermal pressurization dominant, $\dot{\mu}$ changes sign to become strengthening with about $3d_c$ (0.3 mm) additional slip. After that time, thermal pressurization drives the fault weakening such that $\dot{\theta}/\theta$ is much less than the acceleration $\dot{v}/v$. Thus, the direct velocity effect (the a term in the friction law [4]) causes friction $\dot{\mu}$ to become strengthening; in other words, frictional state cannot "keep up" with the acceleration. We also note that radiation damping starts to grow in importance at a slip of ~$33d_c$, but that it is still several orders of magnitude weaker than any other effect until ~$40d_c$, which corresponds to $v_{max} \approx 0.1$ m/s.

[36] During the nucleation phase, the fault accumulates relatively modest slip and temperature rise by the time that thermal pressurization dominates frictional weakening. Figure 4a illustrates profiles of cumulative slip corresponding to the same snapshots in Figure 2. The slip profiles are similar to isothermal, drained nucleation (not shown) with the exception of a small amount of localized slip visible at the center of the nucleation zone in snapshots corresponding to high slip speeds. As inferred from Figure 3, thermal pressurization dominates the fault weakening after only 3.4 mm of slip has occurred. The corresponding temperature rise is only about 3.5°C (Figure 4b). With the p-T relationship for the zero-width shear zone (16), that corresponds to a pore pressure increase of 1.4 MPa, which is only 1% of the initial effective normal stress.

3.2. Critical Velocity

[37] We quantify the critical velocity for thermal pressurization v_{crit} as the peak velocity on the fault at the time when $|\mu_0\dot{p}| = |\dot{\mu}(\sigma - p_0)|$. In defining v_{crit}, we neglect the second-order quantities $(\mu - \mu_0)\dot{p}$ and $\dot{\mu}\Delta p$ for ease of analysis and because they are small compared to $\mu_0\dot{p}$ and $\dot{\mu}(\sigma - p_0)$. For a single point, the definition of v_{crit} is straightforward, but for a continuum there is some spatial variability of which effect dominates the fault strength. We

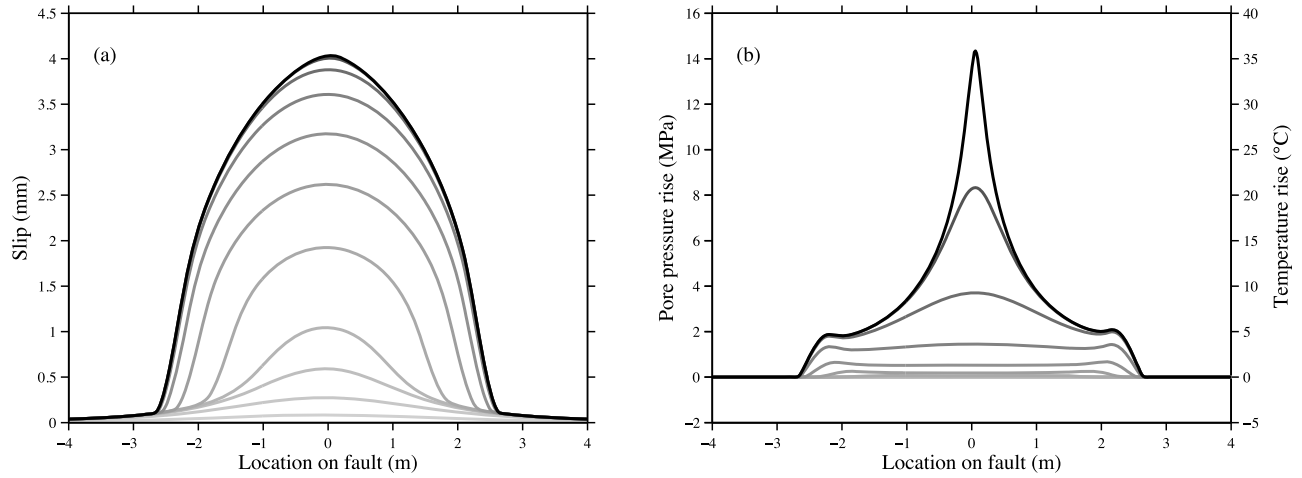

Figure 4. (a) Snapshots of cumulative fault slip during nucleation with thermal pressurization. Snapshots correspond to those in Figure 2. (b) Snapshots of pore pressure and temperature on the fault, which are uniquely related through equation (16).

therefore integrate the aforementioned terms over all regions on the fault that have weakened by either mechanism. At each time step, we compare the magnitudes of

$$M_{\text{tp}} = -\int_{\mathcal{L}(t)} \mu_0 \frac{\partial p}{\partial t}\, dx \quad \text{and} \\ M_{\text{fric}} = \int_{\mathcal{L}(t)} (\sigma - p_0) \frac{\partial \mu}{\partial t}\, dx \ , \tag{36}$$

where $\mathcal{L}(t)$ is the region of x for which $\dot{\tau}_f$ is negative or was negative at times prior to t. That domain of integration is somewhat arbitrary, but a more physically motivated definition of v_{crit} or weighting of the integrand would only change its value by a small factor. We define the critical velocity to be

$$v_{\text{crit}} \equiv \left[v_{\max} \text{ when } M_{\text{tp}} < M_{\text{fric}} \text{ for the first time} \right] . \tag{37}$$

Figure 5 shows graphically the determination of v_{crit}. With parameters used in Figure 2, the critical velocity is 6×10^{-5} m/s, which is far below seismic slip speeds. We note that before v_{crit} is attained, thermal pressurization already dominates at the center of the nucleation zone. There, $\dot{\mu}(\sigma - p_0) = -\mu_0 \dot{p}$ at $v_{\max} = 3 \times 10^{-5}$ m/s.

3.3. Shrinking Nucleation Zone

[38] As discussed in section 3.1, thermal pressurization causes the nucleation zone to shrink for slip speeds above v_{crit}, and it eventually evolves to a singularity in nucleation length. This can be understood by noting that $\dot{p} \propto v_{\max}^{3/2}$. This relationship was predicted by *Segall and Rice* [2006], equation 55 based on the rate of heat production ignoring the change in frictional resistance due to pressurization, and is seen in Figure 5 here (see also section 5.2). Thus, $\dot{\tau} \propto -v^{3/2}$, which implies that

$$\frac{\partial \tau}{\partial v} \propto -\frac{v^{3/2}}{\dot{v}} \ . \tag{38}$$

In aging law nucleation, both v and $\dot{v}$ are always positive, so friction on the fault is directly velocity weakening once thermal pressurization dominates. A linear stability analysis near steady state [e.g., *Segall* 2010, pp. 335–336] shows that for pure velocity weakening friction a perturbation δv grows according to

$$\delta v(t) = \exp\left(-\frac{kt}{\frac{\partial \tau}{\partial v}\big|_{v_0}} \right) , \tag{39}$$

where k is the stiffness of the loading system. In an elastic medium, stiffness is inversely proportional to the length of the slipping zone and is always positive. Since the argument of equation (39) is always positive, any velocity perturbation will grow to instability, regardless of how large k (or small L) is. In short, elasticity alone cannot stabilize a shrinking nucleation zone on a zero-width fault weakening by thermal pressurization.

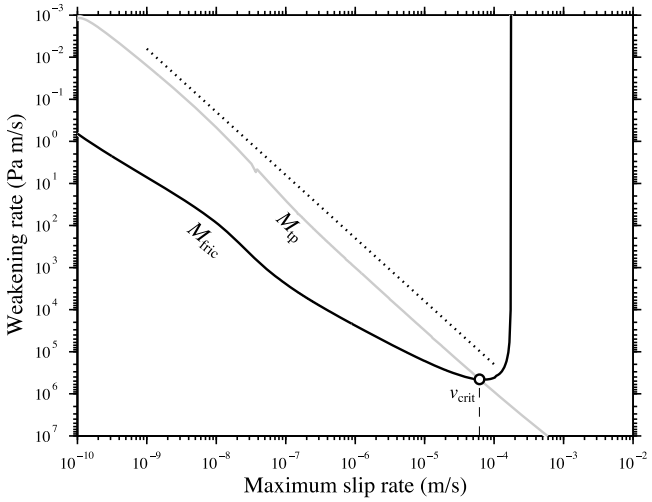

Figure 5. Evolution of the weakening rate within the nucleation zone with aging law friction and thermal pressurization. Critical velocity v_{crit} is shown by the vertical dashed line and is defined when $M_{\text{tp}} = M_{\text{fric}}$ (see equation (36)). The dotted line has a slope of −3/2 for reference.

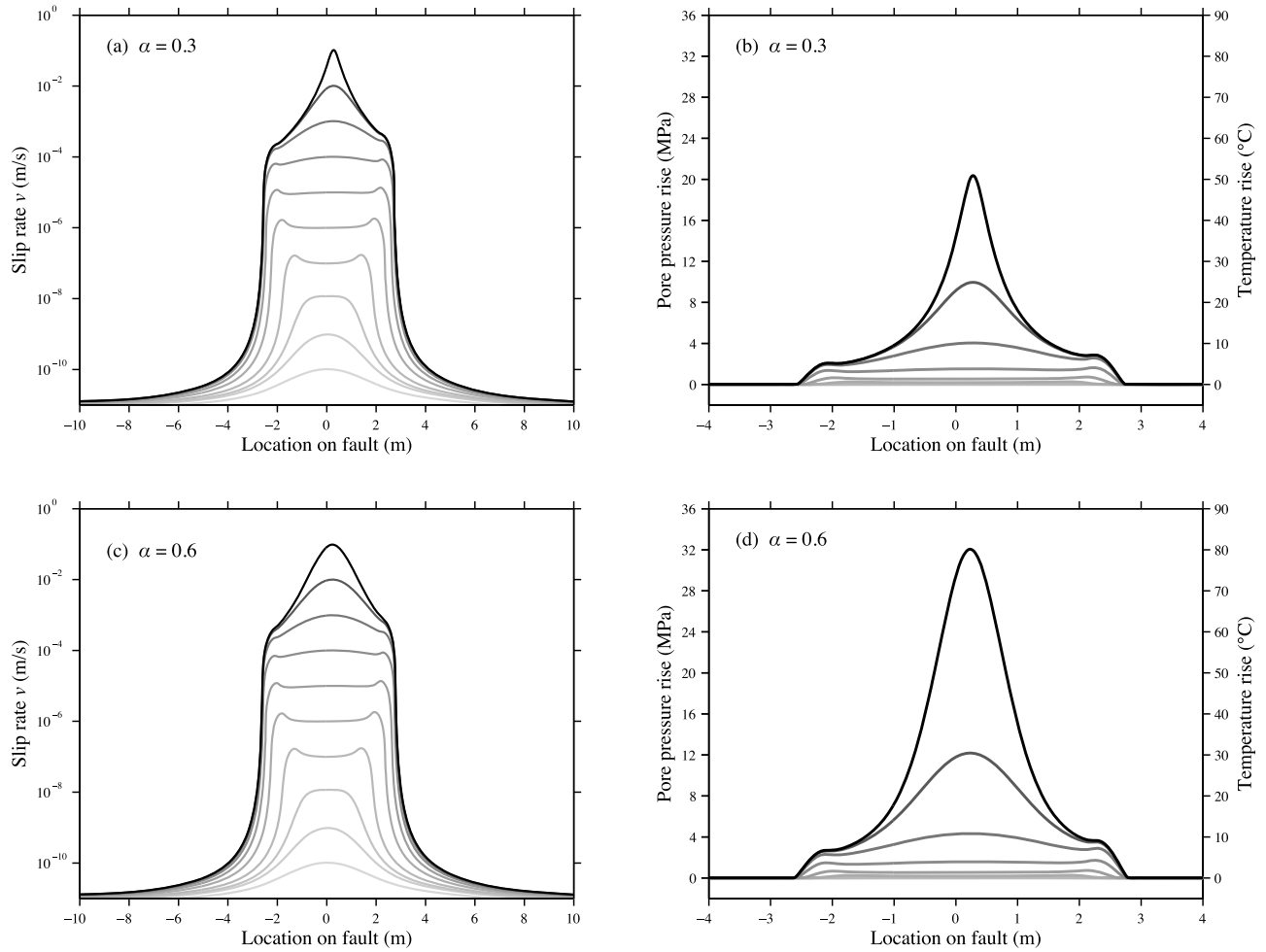

Figure 6. Results of two simulations of aging law nucleation with thermal pressurization including the *Linker and Dieterich* [1992] effect. These simulations were started with identical initial conditions as those of Figure 2, which neglects the effect ($\alpha = 0$). (a) Snapshots of slip speed with $\alpha = 0.3$. The active slipping region shrinks less than with $\alpha = 0$. (b) Snapshots of temperature and pressure the same times as Figure 6a. (c) Slip speed profiles with $\alpha = \mu_0 = 0.6$, showing even less localization. (d) Snapshots of temperature and pressure corresponding with Figure 6c.

3.4. The Effect of Variable Normal Stress on Frictional State

[39] In the simulations presented above, a change in effective normal stress leads to an immediate change in shear stress on the fault. *Linker and Dieterich* [1992], however, observed in rock sliding experiments that changes in shear stress lag behind changes in normal stress. For sliding at constant velocity with an imposed step change in normal stress, part of the response in shear stress is instantaneous, with the remainder occurring over a small slip distance: a few d_c in the rate-and-state friction framework. *Linker and Dieterich* [1992] presented a constitutive law (7) that is also applicable to continuous changes in effective normal stress and is relevant to the present work.

[40] We tested the influence of the *Linker-Dieterich* effect by conducting simulations with $\alpha = 0.3$ and $\alpha = \mu_0 = 0.6$, keeping all other parameters fixed. *Linker and Dieterich*'s [1992] laboratory studies found values of $0.2 < \alpha < 0.3$, and the end-member case of $\alpha = \mu_0$ serves to place an upper bound on the influence of this effect. Figure 6 compares slip speed and temperature profiles for the two values of α. The most striking effect is that increasing α reduces the extreme localization of slip. In both of the simulations shown in Figure 6, the nucleation zones did not collapse to a zero-length singularity before the simulations' ends. However, we have found that, given sufficient time, $\alpha < \mu_0$ always leads to a zero-length slip singularity provided that radiation damping does not dominate first.

[41] With $\alpha > 0$, the temperature increase is amplified (Figure 6). This is a direct consequence of the influence of shear stress on heat production. Without the *Linker-Dieterich* effect ($\alpha = 0$), an incremental decrease in effective stress leads immediately to a decrease in shear strength. With $\alpha > 0$, there is a delay in the loss of shear resistance. Hence, for similar values of v, the resulting shear stress on the fault is greater, and more shear heating therefore occurs.

[42] Despite the significant effect on nucleation zone shape and fault zone temperature, we find that the *Linker-Dieterich* effect does not significantly affect v_{crit}, the speed

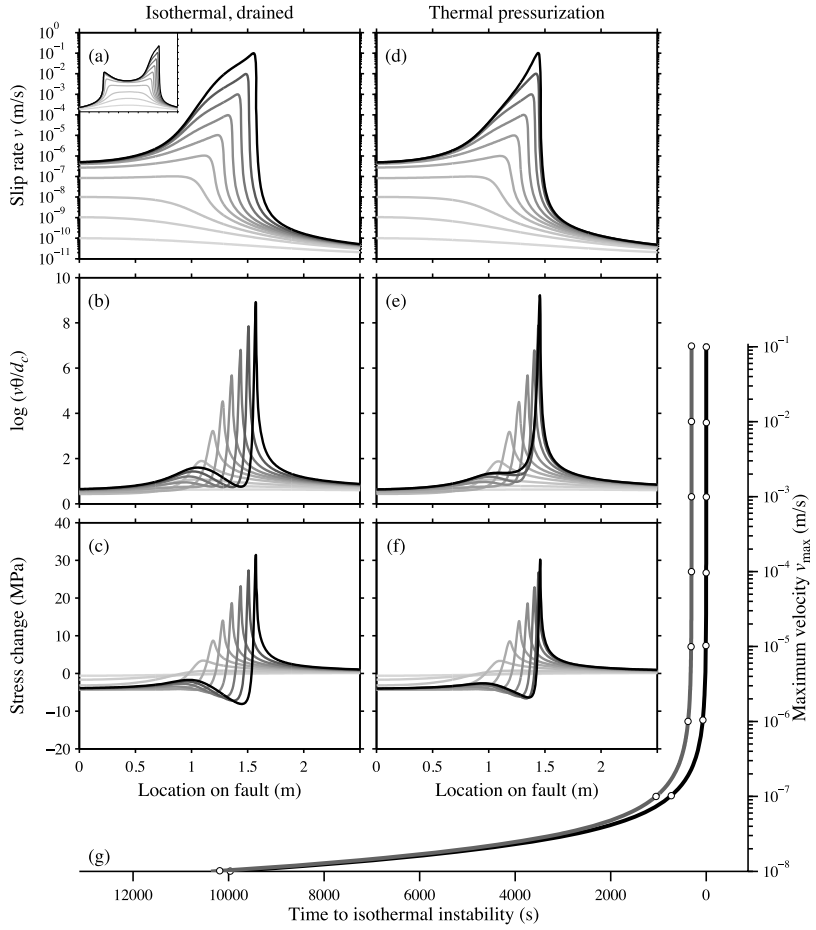

Figure 7. Comparison of slip law nucleation (a-c) without and (d-f) with thermal pressurization. We show the half of the nucleation zone that becomes a slip pulse. Figures 7a and 7d show snapshots of slip speed on the fault. The qualitative difference above 10^{-2} m/s suggests when thermal pressurization begins to dominate fault weakening inside the nucleation zone. When v_{max} is greater than those speeds, thermal pressurization causes the slip pulse to narrow. The inset in Figure 7a shows the entire nucleation zone, including the side that does not develop a sustained slip pulse. Figures 7b and 7e are snapshots of $\log_{10}(v\theta/d_c)$. Figures 7c and 7f are snapshots of frictional resistance to slip. Thermal pressurization suppresses the restrengthening in the trailing region of the slip pulse. Figure 7g shows slip speed in the middle of the nucleation zone over time with and without thermal pressurization. Thermal pressurization only slightly advances the time of the instability. Dots correlate to the snapshots shown in Figures 7a–7f.

at which thermal pressurization dominates. Yet its effect on the nucleation zone geometry indicates that it (or a similar effect such as the one reported by *Prakash and Clifton* [1993]) must be included in fault models with an infinitesimally thin shear zone. A normal stress effect may not be as critical, however, for models that incorporate a finite width shear zone; the diminished temperature rise of such models will reduce the nucleation zone's tendency toward extreme localization.

4. Slip Law Nucleation

4.1. Comparison to Isothermal, Drained Nucleation

[43] Isothermal, drained nucleation with the slip law is markedly different than with the aging law. Near steady state, both exhibit the same response to perturbations in slip speed, so both have an initial slip-weakening phase with length scale L_{min}. As slip accelerates, however, slip law nucleation takes the form of a unidirectional slip pulse, rather than the crack-like character associated with the aging law (Figure 7a). One tip of the slip zone begins to propagate faster than the other, and eventually becomes an accelerating slip pulse. A healing zone trails behind the slip pulse, restrengthening the fault to a new (but lower than initial) stress state.

[44] A feature of pulse-like nucleation is that the maximum slip speed occurs at the leading edge of the nucleation zone, in an area with little cumulative slip. Since thermal pressurization is effectively a slip-weakening process, its influence is significantly reduced for slip law friction compared to aging law friction (as noted by *Ampuero and Rubin* [2009]). Yet our numerical simulations indicate that thermal pressurization still eventually dominates weakening under a range of conditions. In Figure 7 we compare a simulation of isothermal, drained, slip law nucleation with one that includes thermal pressurization, keeping all other parameters identical

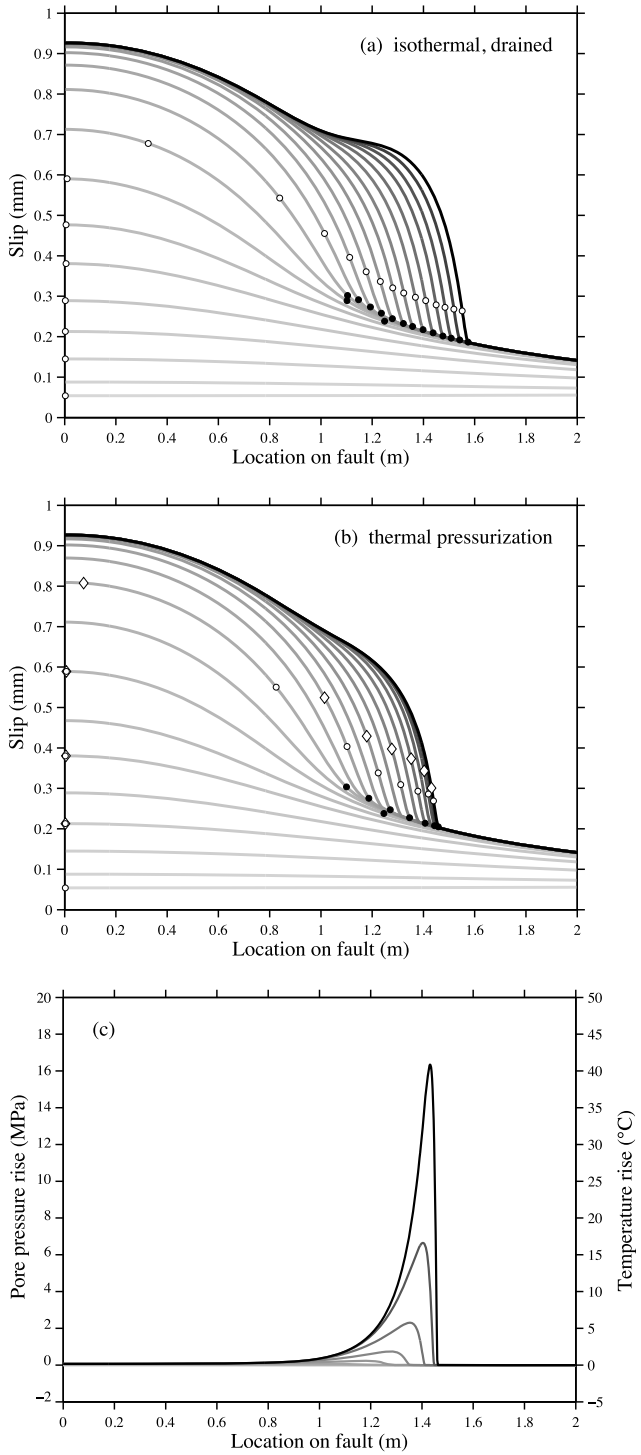

Figure 8. (a) Snapshots of cumulative slip for isothermal, drained slip law nucleation. Snapshots here correspond to half decade increments in v_{max}, so every other snapshot corresponds with those shown in Figure 7. White dots indicate the location of v_{max} and black dots indicate the pulse tip location as defined by the stress maximum. (b) Cumulative slip with thermal pressurization. White diamonds indicate the location of maximum pore pressure. For clarity, markers are omitted for the half decade snapshots. (c) Temperature and pore pressure rise on the fault. The half decade snapshots are omitted.

to the aging law simulations described above (and with α = 0.6). Much like the aging law simulations, the first several snapshots are identical between the two cases, even as the nucleation pulse develops. Snapshots of slip speed (plots a and d) show that nucleation continues to be pulse like in both cases, but that the pulse shape is qualitatively different at higher slip speeds (in this example, the deviation occurs for snapshots with $v_{max} > 10^{-2}$ m/s, which corresponds roughly to v_{crit}). With thermal pressurization, slip speed decays over a much shorter distance behind the pulse tip. In other words, thermal pressurization leads to a smaller pulse width for corresponding maximum slip speeds. As in aging law nucleation, thermal pressurization causes the frictional instability to occur at a slightly earlier t_{inst}, though the time advance is proportionally smaller at about 5×10^{-7} of the time it takes for slip to nucleate from below steady state conditions.

[45] Figure 8 shows cumulative slip in relation to the location of v_{max} and the peak stress, which defines the pulse tip. Early in nucleation, the maximum pore pressure occurs at the point of maximum slip, but as the pulse accelerates, the pressure maximum quickly moves to the location of v_{max}.

[46] The amount of heating is a convolution of frictional work with a diffusion kernel [e.g., *Carslaw and Jaeger*, 1959],

$$T(y=0,t) = \frac{1}{2\rho c_v \sqrt{\pi c_{th}}} \int_0^t \frac{\tau(t')v(t')}{\sqrt{t-t'}}\, dt' \,. \qquad (40)$$

When v_{max} is stationary and continuously increasing, the integral in equation (40) is maximal at the location of maximum slip. In a pulse-like regime, however, v becomes concentrated at the pulse tip, where little prior slip has occurred. In this case, the integral in equation (40) is dominated by the recent slip rate history, such that the maximum temperature is located near the current v_{max} (Figure 8b). Given sufficiently high slip speeds, thermal pressurization still ultimately dominates fault weakening. At $v_{max} > v_{crit}$, the dominant weakening occurs behind the pulse tip, which leads to a slowing of the pulse that we consider in detail in section 4.2.

[47] Because slip law nucleation is a moving pulse, we use a slightly different definition of v_{crit} than in section 3.2. Instead of integrating the weakening effects over all regions that have weakened at prior times, here we only consider the regions weakening at the current time: and only in the active pulse. That is, we compare the magnitudes of M_{tp} and M_{fric} according to equations (36) and (37), but where $\mathcal{L}(t)$ is now defined as the region of x in the active pulse with negative $\partial\tau_{fric}/\partial t$ at time t. Figure 9a shows the determination of v_{crit} with this method. The jog at $v \approx 3 \times 10^{-7}$ m/s corresponds to the formation of a pulse at the end of the initial slip-weakening phase.

[48] Because of the reduced effect of thermal pressurization relative to aging law nucleation, v_{crit} is higher in slip law nucleation. We find that, for the parameters used here, $v_{crit}^{\text{slip law}} \approx 100 v_{crit}^{\text{aging law}}$. While significantly higher, we emphasize that v_{crit} is still at or below seismic slip speeds for a range of realistic hydraulic diffusivities (discussed in section 5.5), including that which is used in the current simulation ($c_{hyd} = 10^{-6}$ m^2/s).

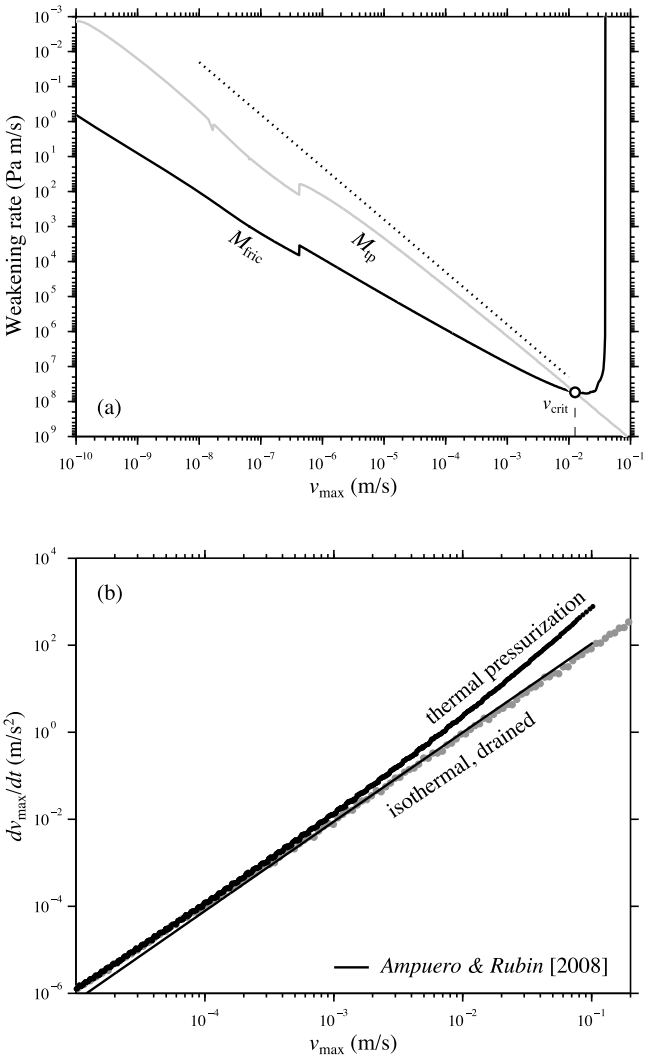

Figure 9. (a) Weakening rates for slip law nucleation, as given by equation (37) and presented in the same fashion as Figure 5. The critical velocity v_{crit} is marked. (b) Slip acceleration. As v_{max} approaches v_{crit}, slip accelerates faster with thermal pressurization than in the isothermal, drained case. The solid line shows the prediction of equation (41) [*Ampuero and Rubin*, 2008] given the values of v_{max} and θ_{bg} in the simulation with thermal pressurization. It agrees with the isothermal result, but not the result with thermal pressurization.

[49] An expected consequence of rate- and state-dependent friction under isothermal, drained conditions is that slip acceleration $\dot{v}$ is proportional to v^2. In aging law nucleation with the no-healing approximation ($\dot{\theta} \approx -v\theta/d_c$) and fixed length nucleation ($\dot{\tau} \approx -k\dot{v}$ with constant k), this leads to an ODE of the form $\dot{v} = Cv^2$ [*Dieterich*, 1992]. With the slip law, however, behavior is more complex. *Ampuero and Rubin* [2008] observed in their simulations of isothermal slip law pulses that slip acceleration $\dot{v}_{max}$ is proportional to v_{max}^2 and the frictional state ahead of the pulse, and satisfies

$$\frac{dv_{max}}{dt} = \frac{Cv_{max}^2}{d_c} \ln \frac{v_{max}\theta_{bg}}{d_c} , \qquad (41)$$

where θ_{bg} is the frictional state ahead of the pulse and C is an empirical constant. When thermal pressurization is included, $\dot{v}_{max}$ deviates from equation (41), which is shown in Figure 9b. In fact, $\dot{v}_{max}$ at v_{crit} is about double the value predicted by equation (41). For comparison, $\dot{v}_{max}$ for an isothermal simulation with identical initial conditions is plotted; it corresponds well with equation (41). The heightened slip acceleration at $v_{max} > v_{crit}$ is simply a consequence of the fact that thermal pressurization is weakening the fault faster than in the drained case.

[50] Figures 7c and 7f illustrate how thermal pressurization affects the stress behind the pulse tip. In the isothermal, drained case, there is a stress minimum behind the tip with a total stress drop proportional to ln v_{max}. Thermal pressurization causes smaller stress drops for a given slip speed, or put another way, slip rates are higher for a given stress change. This behavior is consistent with the enhanced acceleration noted in Figure 9b.

4.2. Nucleation Pulse Propagation

[51] In Figures 7 and 8, it is clear that thermal pressurization affects the slip pulse propagation during slip law nucleation. Since the distribution of shear stress and frictional state following nucleation influences subsequent seismic rupture, pulse propagation bears further examination. Figure 8 shows that, with thermal pressurization, the pulse propagates a shorter distance than in the isothermal case for the same values of v_{max}. In Figure 10a, we plot pulse position as a function of time remaining to instability, t_{inst}; thermal pressurization clearly reduces the distance the pulse propagates. At early times (larger $t_{inst} - t$), the pulses in both cases have similar trajectories, which indicates that the total duration of pulse-like nucleation is roughly equal between the isothermal, drained case and the case with thermal pressurization. Careful examination (not shown in Figure 10) reveals that thermal pressurization shortens the pulse duration by a tiny amount by both delaying its formation (by up to 10^{-5} of the pulse duration) and advancing the instability (Figure 7g; about 10^{-4} of the pulse duration).

[52] Since thermal pressurization decreases the propagation distance while keeping the pulse duration roughly constant, it also diminishes the pulse propagation velocity. In Figure 10b, a substantial slowing of the pulse propagation speed is visible for $v_{max} > v_{crit}$. *Ampuero and Rubin* [2008] noted that the pulse tip propagation speed follows

$$v_{max} = -\frac{dx_{pulse}}{dt}\frac{d\delta}{dx}\bigg|_{x(v_{max})} , \qquad (42)$$

where δ is the cumulative slip and its gradient is evaluated at the location of maximum slip speed v_{max}. This relationship is generally valid for a translating pulse as long as the slip gradient at the tip changes more slowly than the pulse propagates, and is shown schematically in Figure 10c. *Rubin and Ampuero* [2009] observe that the slip gradient changes very little compared to $\dot{x}_{pulse}$, and we find that thermal pressurization does not change that fact (Figure 10d) despite having a small effect on the slip gradient.

[53] The reason thermal pressurization slows the pulse propagation velocity can now be understood. Thermal

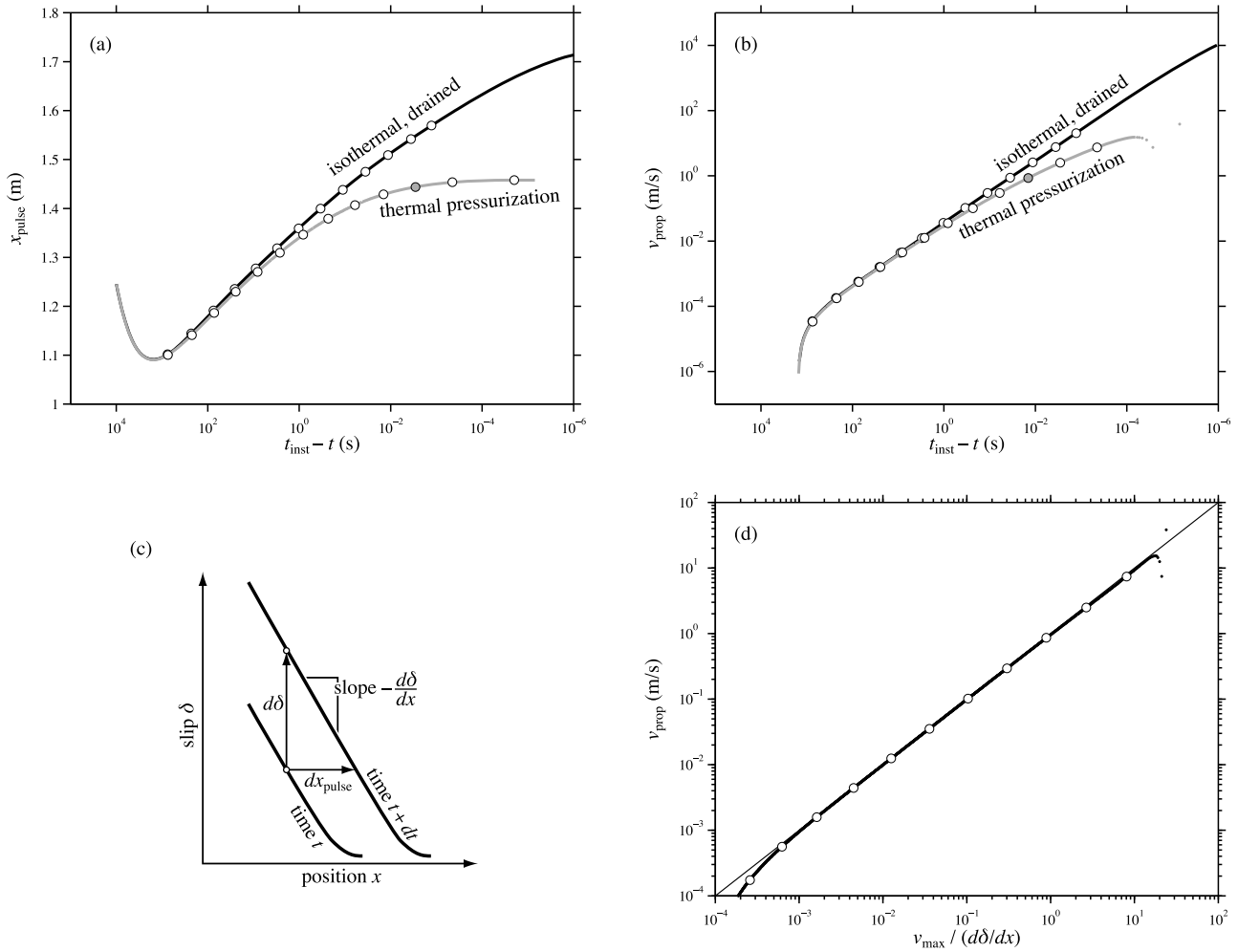

Figure 10. (a) Slip law pulse position at times before t_{inst}. Dots correspond to snapshots in Figure 7. The early backwards motion is the stress maximum moving inward during the initial slip-weakening phase. The gray dot corresponds to v_{crit}. (b) Pulse propagation velocity. The roll-off when t_{inst} is imminent indicates a loss of numerical precision. (c) Schematic illustrating equation (42), the relationship between pulse propagation velocity, slip speed, and slip gradient. (d) Thermal pressurization satisfies equation (42), which is shown by the solid line.

pressurization increases slip acceleration $\dot{v}_{max}$ for a given v_{max} (Figure 9b). At any given time to instability ($t_{inst} - t$), a greater $\dot{v}_{max}$ implies that v_{max} must be less; if the fault is accelerating faster yet reaches instability at nearly the same time, the instantaneous velocity must be less. Hence, from equation (42), a lower value of v_{max} implies that $\dot{x}_{pulse}$ is smaller with thermal pressurization.

5. Effects of System Parameters

5.1. Analytic Prediction

[54] To guide our exploration of the dependence of thermal pressurization on the various system parameters, we first write an analytical expression for thermal pressurization. Following *Segall and Rice* [2006], we start with equation (40), the expression for shear heating on the boundary of a diffusive body. We next assume that, at least initially, the stress does not vary significantly (that is, that the stress change is much less than the total shear stress on the fault), so that for the purpose of this estimate, $\tau \approx \mu_0(\sigma - p_0)$. Using equation (16), we obtain the pore pressure on the fault as,

$$p(y=0,t) \approx \left[\frac{\Lambda\mu_0(\sigma - p_0)}{2\rho c_v\left(\sqrt{c_{th}} + \sqrt{c_{hyd}}\right)}\right]\frac{1}{\sqrt{\pi}}\int_0^t \frac{v(t')}{\sqrt{t-t'}}\,dt' \quad , \quad (43)$$

in which the bracketed term serves as a coefficient that controls the intensity of pressurization resulting from an arbitrary slip rate history. As mentioned in section 3.2, the critical velocity v_{crit} is a convenient measure of the intensity of thermal pressurization: if thermal pressurization is strong, it dominates at lower slip speeds. The definition of v_{crit} in equation (37) includes nucleation zone geometry,

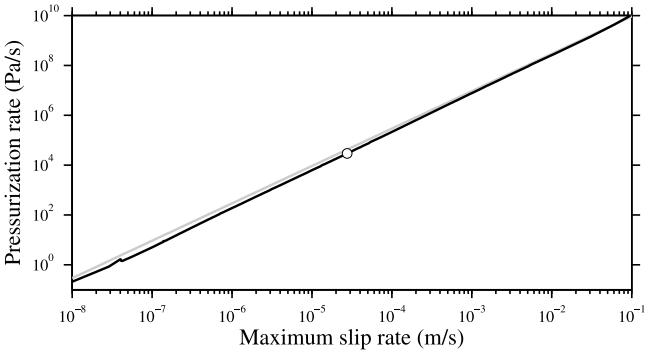

Figure 11. Comparison of dp/dt predicted by equation (49) (gray) and the numerical results for an aging law simulation with $a/b = 0.8$ (black). The dot corresponds to v_{crit}.

which complicates analysis of equation (43). A simpler pointwise definition that we adopt in this section is

$$v_{\mathrm{crit}} = v_{\mathrm{max}} \quad \text{when} \quad \mu_0 \dot{p} = -(\sigma - p_0)\dot{\mu} \quad \text{at the location of } v_{\mathrm{max}}. \tag{44}$$

All references to velocity in this section refer to v_{max}; for simplicity, we shall omit the subscript $_{\mathrm{max}}$.

5.2. Dependence on a and b: Aging Law

[55] With the aging form of the state evolution law (5), analytical expressions [*Dieterich*, 1992; *Rubin and Ampuero*, 2005; *Ampuero and Rubin*, 2008] can be written to describe the slip history of an isothermal nucleation zone, which may then be used to approximate $v(t)$ in equation (43). *Segall and Rice* [2006] present that analysis for a nucleation zone of fixed length, which they took to be L_{min} (equation (25)). To define the critical slip speed v_{crit}, they compare the rate of thermal weakening $-\mu_0 \dot{p}$ to the elastic unloading rate $\dot{\tau} = -d(k\delta)/dt$ that would occur in the absence of thermal pressurization.

[56] We derive a similar estimate, but informed by the results of *Ampuero and Rubin* [2008] for aging law nucleation. The maximum slip speed in aging law nucleation is given by

$$v(t) = \left[\frac{1}{v_i} - \frac{H(a,b,d_c)t}{a}\right]^{-1}, \tag{45}$$

where v_i is the initial slip speed and H is a quantity that controls the slip acceleration (larger H leads to earlier instability and greater acceleration prior to instability). Based on the results of *Rubin and Ampuero* [2005], an estimate of H is

$$H = \begin{cases} \dfrac{(\pi-2)b}{\pi d_c} & \text{for } \dfrac{a}{b} \le \dfrac{\pi-2}{\pi} \\ \dfrac{\pi}{2d_c}(b-a)\dfrac{a}{b} & \text{for } \dfrac{\pi-2}{\pi} \le \dfrac{a}{b} < 1 \end{cases}. \tag{46}$$

The expression for H for low a/b is slightly different than that of *Rubin and Ampuero* [2005]; using numerical methods, they found $H \approx 0.3781 b/d_c$, which differs from equation (46) by 4%. We chose to use algebraic expressions in π for mathematical simplicity, since these expressions are only approximations. For the special case of $a/b = (\pi - 2)/\pi$, equation (46) simplifies to $H = a/d_c$, which is *Dieterich*'s [1992] expression for nucleation of a zone of fixed length L_{min} under the no-healing approximation. *Segall and Rice* [2006] use this value of H in their estimate of v_{crit}. Substituting equation (45) into equation (43) and evaluating the integral leads to

$$p(y=0,t) \approx \frac{\Lambda\mu_0(\sigma - p_0)\sqrt{av}}{\rho c_v\left(\sqrt{c_{\mathrm{th}}} + \sqrt{c_{\mathrm{hyd}}}\right)\sqrt{\pi H}} \arctan\sqrt{\frac{v}{v_i} - 1}\ . \tag{47}$$

In most cases, $v \gg v_i$ so the arctangent evaluates to $\pi/2$. We note from equation (45) that

$$\frac{dv}{dt} = \frac{H}{a}v^2\ , \tag{48}$$

so the pressurization rate is therefore

$$\left.\frac{dp}{dt}\right|_{(y=0,t)} \approx \frac{\Lambda\mu_0(\sigma - p_0)\sqrt{\pi H v^3}}{4\rho c_v\left(\sqrt{c_{\mathrm{th}}} + \sqrt{c_{\mathrm{hyd}}}\right)\sqrt{a}}\ , \tag{49}$$

which is exactly equation (55) of *Segall and Rice* [2006]. In Figure 11, we demonstrate that equation (49) is a very good estimate by comparing it with $\dot{p}$ from the simulation shown in Figure 6 (with $a/b = 0.8$).

[57] To estimate v_{crit}, we compare equation (49) to the frictional weakening rate $\dot{\mu}(\sigma - p_0)$. This approach neglects the feedback of pressurization into slip acceleration, but remains instructive. In the absence of inertial effects, frictional weakening is equal to the decrease in driving stress. Under drained conditions

$$(\sigma - p_0)\frac{d\mu}{dt} = -\frac{d}{dt}(k\delta) = -\delta\frac{dk}{dt} - kv\ . \tag{50}$$

In general, the stiffness of a slipping zone is inversely proportional to its length; that is, $k \propto G/2L$, where L is the half length of the zone. Assuming unit proportionality, equation (50) becomes

$$(\sigma - p_0)\frac{d\mu}{dt} = \frac{G}{2L}\left(\frac{\delta}{L}\frac{dL}{dt} - v\right)\ . \tag{51}$$

The critical half length for rate/state friction is

$$L = \frac{G d_c}{2\sigma_{\mathrm{eff}} f(a,b)}\ , \tag{52}$$

where $f(a, b)$is different for L_{min}, L_ν, or L_∞. We define v_{crit} as the slip speed, v, for which $\mu_0\dot{p} = -(\sigma - p_0)\dot{\mu}$. The nucleation zone's growth rate $\dot{L}$ is proportional to the slip speed inside the zone ($\sim v$) and slip gradient $d\delta/dx$ (similar to equation (42)); since $|d\dot{\delta}/dx| \gg \dot{\delta}/L$ near the tip of a slip zone, we find $\dot{\delta}\dot{L}/L \ll v$. With that approximation, equations (49), (51), and (52) yield

$$v_{\mathrm{crit}} \approx \frac{a[f(a,b)]^2}{\pi H}\left[\frac{4\rho c_v\left(\sqrt{c_{\mathrm{th}}} + \sqrt{c_{\mathrm{hyd}}}\right)}{\Lambda d_c \mu_0^2}\right]^2 \tag{53}$$

for which we can select different values of $f(a, b)$ and H for the different aging law nucleation regimes.

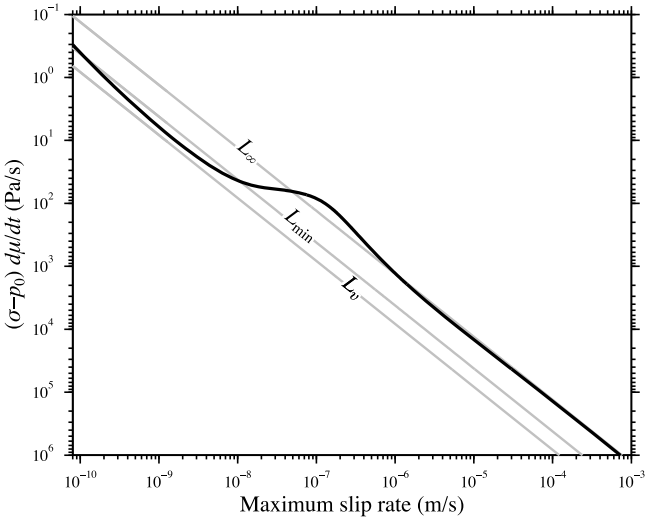

Figure 12. Weakening rate during isothermal nucleation, which is described by equation (51). Straight lines correspond to the decrease in stress due to slip in fixed width nucleation zones. The numerical result of the isothermal, drained nucleation zone of Figure 2 is shown. The nucleation zone initially weakens in a zone of length $2L_{\min}$, then contracts toward a length of $2L_\nu$, and finally expands toward a length of $2L_\infty$.

[58] *Segall and Rice* [2006] chose $H = a/d_c$ and $f(a, b) = b - a$ (corresponding to $L_{\min}$) to obtain

$$v_{\text{crit}}^{\text{SR06}} \approx \frac{1}{\pi d_c}\left[\frac{4\rho c_v (b-a)\left(\sqrt{c_{\text{th}}}+\sqrt{c_{\text{hyd}}}\right)}{\Lambda\mu_0^2}\right]^2 . \qquad (54)$$

We note, however, that the value of H given by equation (46) is more appropriate in the later phase of nucleation. We also choose $f(a, b)$ as appropriate for the phase of nucleation and the a/b regime. The initial slip phase has half length $L_{\min}$, but slip then localizes approaching dimension L_ν. For $a/b > 0.5$, the nucleation zone then grows toward half length L_∞. This evolution can be seen in Figure 12, which corresponds to the isothermal, drained simulation shown in Figure 2. Following equation (46) and *Rubin and Ampuero* [2005], we use the following expressions for $f(a, b)$:

$$f(a,b) = \begin{cases} \dfrac{\pi b}{8} & \text{for } \dfrac{a}{b} \le \dfrac{1}{2}, \text{ for } L = L_\nu \\ \dfrac{\pi(b-a)^2}{2b} & \text{for } \dfrac{a}{b} \ge \dfrac{1}{2}, \text{ for } L = L_\infty . \end{cases} \qquad (55)$$

As with the approximations for H (see equation (46)), we substitute an approximate expression that is algebraic in π and piecewise continuous over ab^{-1} (compare to equation (34) for L_ν). The expressions in equation (55) correspond to nucleation zones that have attained their final sizes, which is not necessarily the case when $v_{\max} = v_{\text{crit}}$ but still provides a reasonable estimate. Combining equations (46), (53), and (55) yields

$$v_{\text{crit}}^{\text{aging}} = \frac{1}{\pi d_c}\left[\frac{4\rho c_v\left(\sqrt{c_{\text{th}}}+\sqrt{c_{\text{hyd}}}\right)}{\Lambda\mu_0^2}\right]^2 \times \begin{cases} \dfrac{\pi^3 ab}{64(\pi-2)} & \text{for } 0 < \dfrac{a}{b} \le \dfrac{\pi-2}{\pi} \\ \dfrac{\pi b^3}{32(b-a)} & \text{for } \dfrac{\pi-2}{\pi} \le \dfrac{a}{b} \le \dfrac{1}{2} \\ \dfrac{\pi(b-a)^3}{2b} & \text{for } \dfrac{1}{2} \le \dfrac{a}{b} < 1 . \end{cases} \qquad (56)$$

Figure 13 compares numerical values of v_{crit} to predictions from (56), and shows that they are in general agreement. The analytical prediction is high by a factor of ~2, which we attribute to the fact that it neglects the feedback of increases in p on frictional strength.

5.3. Dependence on a and b: Slip Law

[59] Figure 14 presents numerical values of v_{crit} for various values of a and b with the slip law, using the nominal values for all other parameters. Clearly, thermal pressurization exhibits in two markedly different regimes. For $a/b \lessapprox 0.65$, thermal pressurization dominates at slow slip speeds and exhibits strong dependence on a and b. In this regime, a healing front does not develop behind the tip of the slip zone, so it cannot be described as "pulse like." For $a/b \gtrsim 0.65$, the nucleation zone develops a healing front and is thus pulse like. In this regime, the critical velocity v_{crit} is high and only weakly depends on a and b over a wide range of a/b. Qualitatively, the two regimes are a consequence of the competition between the speed of pulse propagation and the rate of thermal pressurization. To first order, the slip

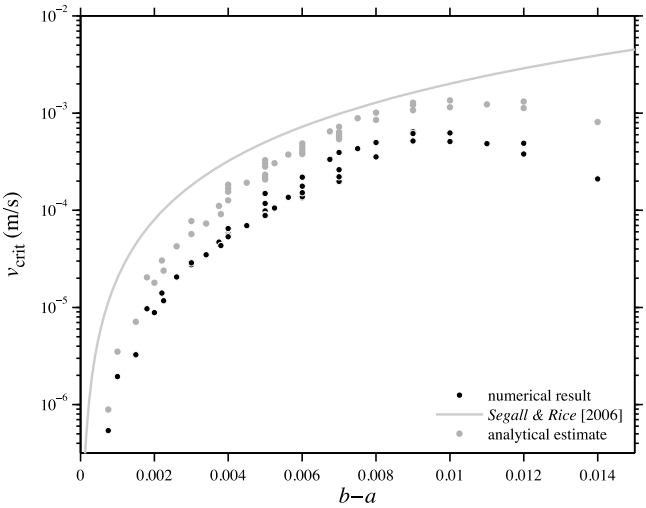

Figure 13. Critical velocity v_{crit} for various a and b in aging law nucleation. Black dots are numerical results. The gray line is the prediction of equation (54) [*Segall and Rice*, 2006]. Gray dots are the predictions of equation (56). Multiple points at a given $b - a$ reflect different values of a/b from 0.263 to 0.95.

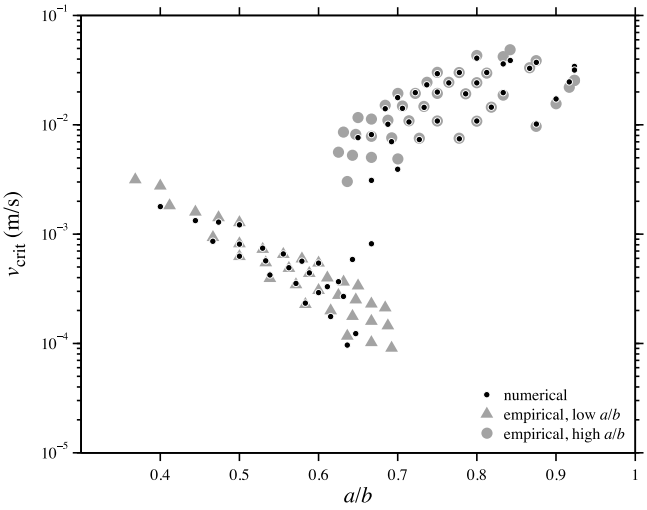

Figure 14. Critical velocity v_{crit} for various a and b in slip law nucleation with thermal pressurization. Black dots are numerical results. Gray triangles and dots are empirical predictions given by equations (57) and (58), respectively. With thermal pressurization, low a/b nucleation is not pulse like.

pulse propagation speed is proportional to $(1 - a/b)^{-2}$ [*Rubin and Ampuero*, 2009] (though its second-order dependence on a and b is considerably more complicated). Hence lower values of a/b lead to slower pulses, which do not propagate fast enough to "outrun" thermal pressurization. On the other hand, high values of a/b lead to rapidly propagating slip pulses for which the zone of greatest weakening occurs in an area with little prior shear heating.

[60] We note that the pointwise definition for v_{crit} (44) and the whole pulse definition (37) can differ significantly for fast pulses. In this case, the point of maximum pressurization follows significantly behind the location of v_{max} (Figure 8b). Consequently, when equation (44) is satisfied, most of the pulse behind $x(v_{max})$ is already dominated by thermal pressurization. We have found that the pointwise estimate of v_{crit} can be as much as 10 times higher than the whole pulse definition for large a/b. For $a/b = 0.8$, the pointwise value of v_{crit} is about 5 times the whole pulse value.

[61] Because of the highly nonlinear trajectories of v and θ with slip law friction, we have been unable to develop analytical predictions of v_{crit}. For the quasi-stationary nucleation zones of the low-a/b regime, we cannot follow the same method developed in equations (40)–(56) above since explicit expressions for $v(t)$ and L are not known. For the pulse-like nucleation, an appealing approach is to treat the pulse arrival as a Heaviside function, $v(t) = vH(t)$, to derive an expression for $p(y = 0, t)$. Numerical results, however, indicate that the velocity history is considerably more complex than a Heaviside function, with a small amount of precursory acceleration followed by finite acceleration during the risetime.

[62] Despite the lack of an analytical prediction for thermal pressurization with slip law friction, we have found that there is a systematic dependence of v_{crit} on parameters a and b. Using a least squares fit to the numerical estimates of v_{crit} in terms of a, b, and $(b - a)$, we find for the low-a/b regime that

$$v_{crit}^{low} \approx \frac{2(b-a)^3}{\pi a d_c}\left[\frac{4\rho c_v\left(\sqrt{c_{th}}+\sqrt{c_{hyd}}\right)}{\Lambda\mu_0^2}\right]^2 \quad (57)$$

and, for the high-a/b regime,

$$v_{crit}^{high} \approx \frac{200a^9(b-a)}{\pi b^8 d_c}\left[\frac{4\rho c_v\left(\sqrt{c_{th}}+\sqrt{c_{hyd}}\right)}{\Lambda\mu_0^2}\right]^2 . \quad (58)$$

These empirical predictions are shown in Figure 14.

5.4. Slip Weakening Distance d_c

[63] The slip weakening distance d_c is the amount of slip necessary for frictional state to evolve following a change in velocity. During nucleation, this controls the slip distance over which a fault transitions from a high-strength, low-speed condition to a low-strength, high-speed condition. It also influences shear heating by controlling how much slip must occur for a given decrease in frictional resistance. Higher values of d_c cause the sliding to occur at high friction for longer slip such that more frictional work is done. Further, large values of d_c correspond to a modest frictional weakening rate, thereby allowing thermal pressurization to dominate earlier. In equation (56), $v_{crit} \propto d_c^{-1}$, which agrees with simulations for small d_c shown in Figure 15.

[64] Interestingly, however, the dependence of v_{crit} changes as d_c gets larger. We attribute this behavior to the fact that large values of d_c cause thermal pressurization to dominate during the initial slip phase rather than during the growing crack phase. In the general aging law prediction for v_{crit}, equation (53), $f(a, b) = b - a$ and $H = a/d_c$ during the

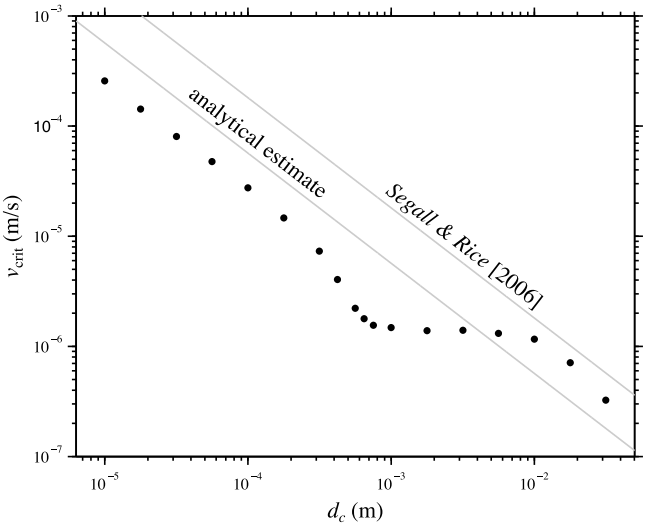

Figure 15. Critical velocity v_{crit} for various d_c in aging law nucleation with thermal pressurization. Black dots are numerical results. The upper gray line is the prediction of equation (54) [*Segall and Rice*, 2006] while the lower gray line is the prediction of equation (56).

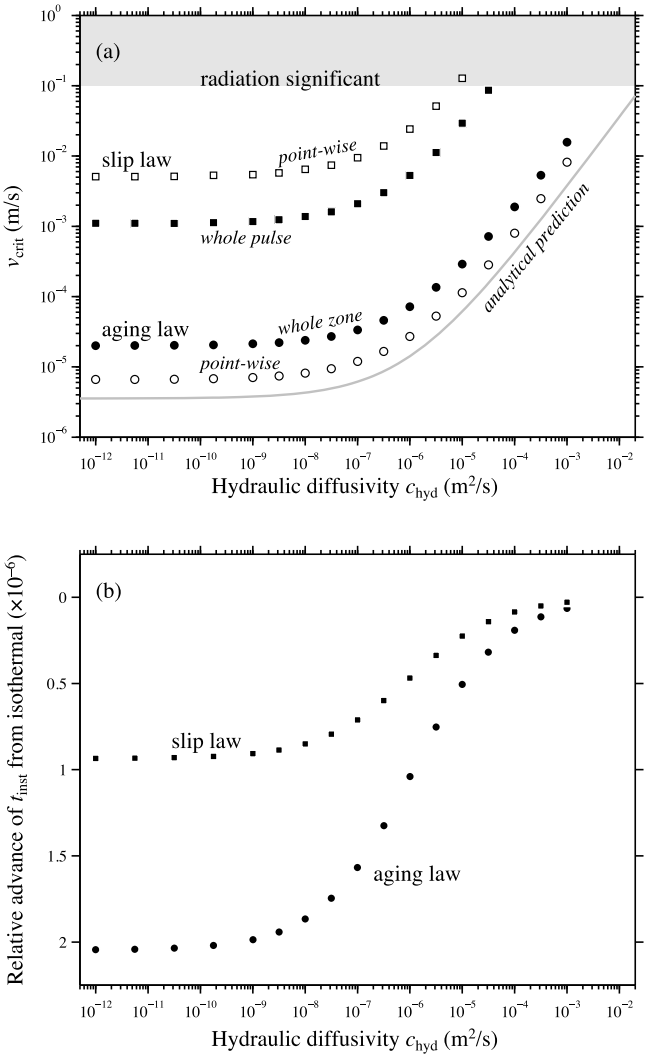

Figure 16. (a) The effect of hydraulic diffusivity c_{hyd} on v_{crit}. All other parameters have nominal values (Table 1). The thermal diffusivity is $c_{th} = 10^{-6}$ m^2/s, so $\mathcal{D}$ ranges from 10^{-4} to 10^{6}. Results from aging law simulations are compared to equation (56). (b) Relative advance of the frictional instability time over the isothermal instability time. The quantity shown is $(t_{inst} - t_{inst}^{isothermal})/t_{inst}^{isothermal}$. Increasing the strength of thermal pressurization advances the time of the frictional instability very modestly. Dots indicate aging law nucleation; boxes indicate slip law nucleation.

initial slip-weakening phase. These expressions for f and H are precisely the assumptions made by *Segall and Rice* [2006] and lead to equation (54), which is plotted in Figure 15. As aging law nucleation transitions from its initial slip-weakening phase (width $2L_{min}$) to its growing crack phase (width approaching $2L_\infty$), the rate/state frictional weakening rate's dependence on v_{max} exhibits a kink as the nucleation zone length changes rapidly (Figure 12). Simulations with d_c values that cause v_{crit} to occur during the transition between nucleation zone lengths thus reflect the kink in $(\sigma - p)\dot{\mu}$ in Figure 12. If laboratory values of d_c (10–100 μm) are applicable at seismogenic depths, however, the large values of d_c shown in Figure 15 would not represent the behavior of natural faults.

5.5. Hydraulic Diffusivity

[65] Of all of the material properties relevant to thermal pressurization, shear zone hydraulic diffusivity c_{hyd} is likely the least well known. For that reason, we tested a broad range of values for both the aging and slip laws. We expect that higher c_{hyd} will reduce the effect of thermal pressurization, since diffusion reduces excess pore pressure in the fault zone. We further expect there to be a limiting value of v_{crit}; even as $c_{hyd} \to 0$, thermal diffusion limits the rate of pressurization.

[66] Values of both pointwise and whole zone/pulse v_{crit} for several numerical simulations are plotted in Figure 16a, and they capture the anticipated dependence on hydraulic diffusivity. For aging law nucleation, the numerical pointwise v_{crit} values agree well with the analytic estimate given by equation (56). Estimates with the whole nucleation zone lead to larger v_{crit} because they include regions that have weakened by rate/state friction but have not undergone as much shear heating. For slip law nucleation, pointwise v_{crit} is roughly three orders of magnitude larger than with the aging law, which is an expected consequence of pulse-like behavior. Unlike aging law nucleation, pointwise values of v_{crit} are larger than whole zone values because the former excludes the portion of the fault with the greatest shear heating (see section 5.3).

[67] As mentioned in sections 3.1 and 4.1, thermal pressurization advances the time of the instability t_{inst} relative to the isothermal case by a modest amount (for a discussion of t_{inst} in the drained isothermal limit, see *Ampuero and Rubin* [2008]). Increasing hydraulic diffusivity reduces the effect of thermal pressurization, and therefore reduces the time advance of instability (Figure 16b). For both aging and slip state evolution laws, there is a maximum advance in t_{inst} in the undrained limit. While a few hundreds of seconds long, both are relatively small compared to the total nucleation time: about 2 parts per million for aging law nucleation and half that for the slip law. Hence thermal pressurization will not significantly bias processes that depend on nucleation time, even for faults with extremely low hydraulic diffusivity.

5.6. Other Parameters: μ_0, Λ, ρ, c_v, and $(\sigma - p_0)$

[68] Although values of the remaining material properties are fairly well constrained from laboratory observations, we tested their influence on thermal pressurization. Equation (43) indicates that the pore pressure increase is directly proportional to the nominal friction coefficient μ_0, and with the aging evolution law, that leads to a prediction of $v_{crit} \propto \mu_0^{-4}$ in equation (56). Qualitatively, lower values of μ_0 correspond to less frictional work for the same amount of slip, thereby reducing thermal pressurization. We find (Figure 17a) that the dependence of v_{crit} on μ_0^{-4} is borne out in numerical simulations. Thermoelastic and poroelastic properties exert a strong influence on thermal pressurization (section 5.5). Equation (56) predicts that v_{crit} scales with $(\rho c_v/\Lambda)^2$. Although this nondimensional group is relatively well constrained [*Rice*, 2006] near the value of 0.28 used throughout this paper, we verify its influence on v_{crit} in Figure 17b.

[69] As indicated by dimensional analysis (32) and, at least for the aging law, the analytical prediction for v_{crit} (56), there is no dependence of v_{crit} on ambient effective stress

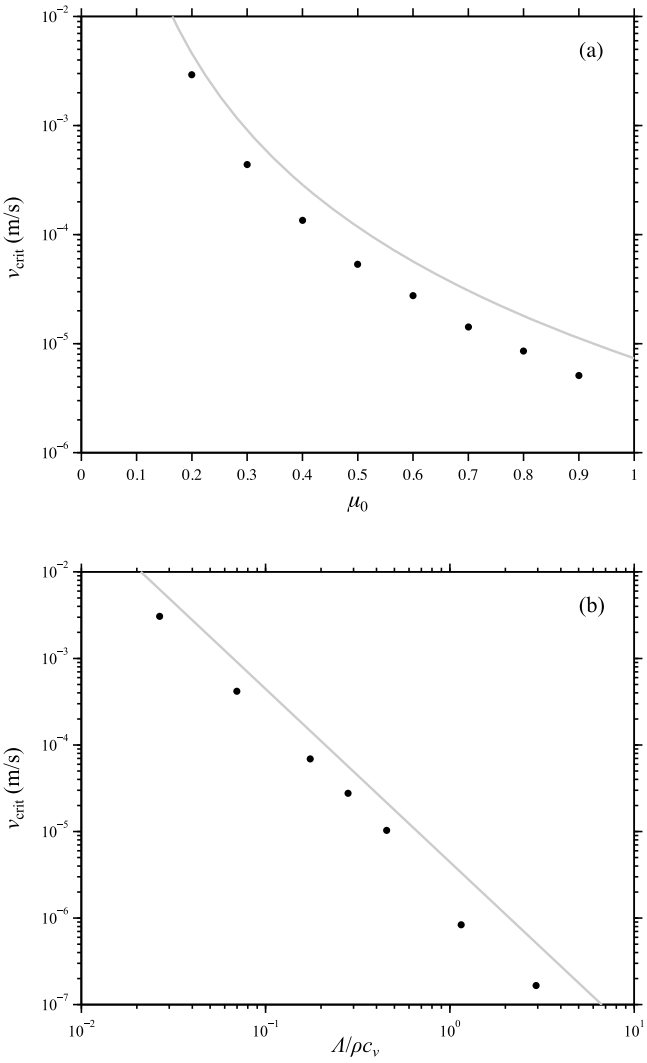

Figure 17. (a) The effect of nominal friction μ_0 on v_{crit}. (b) The effect of $(\Lambda/\rho c_v)$ on v_{crit}. In both plots, dots are numerical results and lines are predictions of equation (56).

$(\sigma - p_0)$, which is confirmed by numerical results. One exception exists: nucleation is affected at extremely low ambient effective normal stress. Since shear heating ceases when $\mu(\sigma - p_0 - p) = 0$, the ambient effective stress imposes an upper bound on the stress drop associated with fault slip. We have not yet investigated models in which a total stress drop occurs during the nucleation phase. Recent studies [e.g., *Audet et al.*, 2009] suggest that near-lithostatic pore pressure is possible at depth in subduction zones, so the issue warrants further consideration.

6. Discussion

6.1. Role of Thermal Pressurization During Nucleation

[70] Our analysis suggest shear heating-induced thermal pressurization is significant (and under many circumstances may be dominant) during the late stages of earthquake nucleation. During the early phase of nucleation on a steady state velocity weakening fault, however, its weakening rate is insignificant compared to the state evolution effect in friction. For that reason, rate/state friction remains necessary to initiate slip instabilities on uniformly loaded faults. In effect, thermal pressurization requires that slip accelerates to a sufficiently high speed that the rate of heat production overwhelms diffusion. Hence thermal pressurization is unlikely to lead to a slip instability on a uniformly loaded, slowly slipping, steady state velocity strengthening fault. *Segall and Rice* [2006] addressed that issue with a linear stability analysis; they showed that even for very small c_{hyd}, perturbations from steady state v are stable for $a > b$. Regardless of the frictional regime, our analysis indicates that thermal weakening effects should be modeled during fault slip at moderate to high quasi-static slip speeds. If, as we suggest, thermal pressurization is significant before dynamic instability, we expect it to be active during both large and small earthquakes. That inference is consistent with the analysis of *Ide and Beroza* [2001], which shows little dependence of apparent stress drop on magnitude for $-3 < M_w < 8$.

6.2. Dilatancy as a Possible Mitigating Effect

[71] While our results argue for the significance of thermal pressurization, we have not considered other mechanical processes that may mitigate its effect. One effect not examined in this paper is dilatancy of shear zone materials, which can counteract the pore fluid expansion and diminish thermal pressurization [*Segall et al.*, 2010]. The interaction can, however, be complex; dilatancy increases the effective normal stress, which in turn leads to enhanced heat production [*Garagash and Rudnicki*, 2003]. Moreover, dilatancy is likely to be dominant only at low effective normal stress. For a given dilatancy rate (that is, rate of increase in porosity) $\Delta\phi$, *Segall et al.* [2010] show that the pressure boundary condition at the fault is (letting $h \to 0$ but keeping $h\dot{\phi}$ nonzero)

$$\left.\frac{\partial p}{\partial y}\right|_{y=0} = \frac{h\dot{\phi}}{2\beta_{\text{eff}} c_{\text{hyd}}} \ . \tag{59}$$

The constitutive law for dilatancy of *Segall and Rice* [1995] (motivated by experiments of *Marone et al.* [1990] is

$$\Delta\phi = -\epsilon \ln \frac{v_0 \theta}{d_c} \ , \tag{60}$$

with laboratory values of ϵ for gouge of $\sim 10^{-4}$. Normalizing as in section 2.3, we obtain a pore pressure boundary condition of

$$\left.\frac{\partial \hat{p}}{\partial \hat{y}}\right|_{\hat{y}=0} = -\mathcal{E}\frac{1}{\hat{\theta}}\frac{d\hat{\theta}}{d\hat{t}} \ , \tag{61}$$

where the "dilatancy efficiency" (called E_p by *Segall et al.* [2010]) is given by

$$\mathcal{E} \equiv \frac{\epsilon}{2\beta_{\text{eff}}(\sigma - p_0)} \sqrt{\frac{h^2 v_\infty}{c_{\text{hyd}} d_c}} \ . \tag{62}$$

In equation (61) it becomes apparent that large effective normal stress reduces the effect of dilatancy. The ratio $\mathcal{E}/\mathcal{F}\mathcal{D}^{1/2}$ measures the relative importance of dilatancy and thermal pressurization. For the nominal parameters used in this study, $\mathcal{E}/\mathcal{F}\mathcal{D}^{1/2} = 0.05$, which indicates that dilatancy is

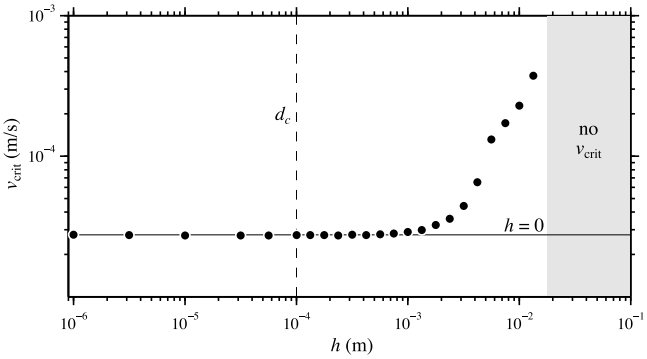

Figure 18. Dependence of v_{crit} on shear zone thickness h for aging law nucleation with parameters otherwise identical to those in Figure 2 ($d_c = 10^{-4}$). For $h \gtrsim 5d_c$, v_{crit} increases with h, which shows that distributed shear should be modeled for such cases.

insignificant compared to thermal pressurization at high effective normal stress. Numerical simulations confirm that result; for example, a simulation with $\epsilon = 10^{-4}$ but otherwise identical to the one shown in Figure 2 yields the same v_{crit}, although the induced pore pressures are ~10% lower. An extensive study of the interaction between dilatancy and thermal pressurization is in progress [*Bradley and Segall*, 2010].

6.3. Distributed Shear

[72] Large shear zone thickness h suppresses thermal pressurization because distributing frictional work over a larger volume diminishes the temperature rise. As discussed in section 2.1, a simple dimensional argument indicates when modeling distributed shear is necessary. Laboratory experiments suggests that h and d_c may be related; rearranging equation (3), we find that distributed shear must be modeled for

$$v(t) \gtrsim \frac{16c}{d_c}\left(\frac{d_c}{h}\right)^2 . \tag{63}$$

Marone and Kilgore [1993] propose $h \approx 100d_c$ based on laboratory friction experiments using simulated fault gouge between steel sliding blocks. *Chambon et al.* [2002] sheared quartz sand and observed shear bands of comminuted particles that were ~60 times larger than the observed d_c. *Rice* [2006] notes that shear bands in granular media are typically 10–20 particles wide, and that d_c likely represents particle size. For $d_c = 100$ μm and $h = 2$ mm, equation (63) suggests that distributed shear must be considered for $v > 4 \times 10^{-4}$ m/s. For $d_c = 10$ μm and $h = 200$ μm, we find $v > 0.004$ m/s. Since these slip speeds are comparable to v_{crit} for a zero-width shear zone, the issue of distributed shear demands further study.

[73] To investigate the effect of shear zone thickness, we performed simulations of aging law nucleation with $d_c = 100$ μm and various shear zone thicknesses h by employing a newer code that integrates separate temperature and pore pressure diffusion grids and is capable of distributed shear heating [*Bradley and Segall*, 2010]. The new code has been validated against the results shown in the rest of this paper. We assume a Gaussian distribution of shear strain rate across a zone with RMS half width $h/2$, given by

$$\frac{d\gamma(x,y,t)}{dt} = \frac{\sqrt{2}v(x,t)}{\sqrt{\pi}h}\exp\left(-\frac{2y^2}{h^2}\right) , \tag{64}$$

which accommodates a total slip speed $v(t)$. Figure 18 shows the effect of distributed shear. For $h \leq 10d_c$, distributed shear had little effect on v_{crit}. For $10d_c < h < 20d_c$ (the favored range of *Rice* [2006]) increasing h leads to increases of v_{crit} of only 10% to 20%, yet the along-strike localization of slip shown in section 3.1 is greatly reduced. For larger shear zone thicknesses, the influence of thermal pressurization weakens dramatically; for $h \gtrsim 50d_c$, thermal pressurization still dominates fault weakening at the location of fastest slip (so v_{crit} is defined), but most of the nucleation zone remains dominated by rate/state friction. For $h \gtrsim 150d_c$, thermal pressurization fails to dominate weakening anywhere on the fault before radiation damping becomes dominant, although it is still a significant contribution to the fault's resistance to shear.

6.4. Effect on Seismicity

[74] An important implication of our simulations is that statistical models of seismicity rates, like that of *Dieterich* [1994], are not significantly affected by thermal pressurization. Such seismicity models depend on the time fault slip takes to become unstable. The time to instability for slip near steady state is

$$t_{inst} - t = \frac{2bd_c}{\pi(b-a)v_{max}(t)} \tag{65}$$

for the aging law with $0.4 < a/b < 1$ [*Ampuero and Rubin*, 2008], and it is of comparable magnitude (but slightly smaller and far more difficult to estimate analytically) for the slip law [*Rubin and Ampuero*, 2009]. For "locked" faults ($\log v_{max} < -12$), the time to instability ($t_{inst} - t$) is several orders of magnitude longer than the ~1000 s advance that results from thermal pressurization (Figure 16b). For that reason, it is not necessary to include thermal pressurization in seismicity rate models that use rate/state friction (for example, the regional earthquake simulator of *Dieterich and Richards-Dinger* [2008]).

[75] The small nucleation zones we observe in our simulations may have implications for detection of the nucleation phase and for estimates of the minimum earthquake magnitude. Recently, researchers have attempted to record the earliest seismic phases of earthquakes by placing strainmeters and seismometers close to faults in deep mines [*Boettcher et al.*, 2009] or in the SAFOD borehole [*Zoback et al.*, 2010]. Under isothermal rate/state friction, nucleation zones have a minimum size at seismic slip speeds. For the aging state evolution law with $0.5 < a/b < 1$, its width is nearly L_∞ (which is perhaps 1.27 to 60 times L_{min}). With thermal pressurization, however, the active slipping zone is much smaller when it reaches seismic slip speeds, and will therefore be much harder to observe with near-source instruments. For isothermal slip law nucleation, the actively slipping region is already small (a fraction of L_{min}) thermal pressurization does not make detection of precursory slip significantly more challenging. In the case of earthquakes that

stop shortly after reaching seismic speeds, thermal pressurization has the potential to decrease the theoretical minimum earthquake size, even for the smallest "picoearthquakes." While identifying thermal pressurization in nature may difficult, future laboratory studies may provide some experimental verification of the numerical results.

7. Conclusion

[76] Our results indicate that weakening during the late earthquake nucleation phase may be dominated by thermal pressurization before seismic slip speeds are attained. Early in nucleation, rate- and state-dependent friction dominates the fault weakening, initiating of a zone of localized fault slip. Rate/state friction continues to dominate the weakening until it transitions to thermal pressurization after sufficient shear heating has occurred. Unless the effective normal stress is low, dilatancy is unlikely to mitigate the pressure rise. For faults with narrow shear zones that can be approximated as a mathematical plane, the transition to thermal pressurization-dominated weakening occurs at different slip speeds for the aging and slip forms of the state evolution law: with $c_{hyd} = 10^{-6}$, the transition is on the order of 0.1 mm/s for the former and 10 mm/s for the latter. Larger fault zone permeability and shear zone thickness raise the slip speed at which the transition occurs. Even with high permeability and slip law friction, thermal pressurization will almost certainly be significant at the earliest stages of earthquake rupture.

Appendix A: Numerical Method

A1. Parameterization

[77] The thermal pressurization analysis requires full coupling of fault friction, elasticity, and diffusion of heat and pore pressure. Using the zero-width shear zone approximation p-T relationship (16), we need only calculate one diffusion field. We compute thermal diffusion, with boundary condition given by equation (11). Elasticity and friction are related through the slip velocity, and friction depends on the state variable. Hence, we have three variables that must integrate in time: slip speed on the fault $v(x, t)$, frictional state $\theta(x, t)$, and temperature in the diffusive domain $T(x, y, t)$.

[78] Because velocity and state vary by many orders of magnitude and are always positive, we find that the following variables are better suited for integration:

$$\psi = \ln\frac{v}{v_0} \tag{A1}$$

$$\chi = \frac{v\theta}{d_c} \ , \tag{A2}$$

which transforms the friction law to

$$\mu = \mu_0 + a\psi + b(\chi - \psi) \ . \tag{A3}$$

With the mapped frictional parameters and temperature discretized in y, we transform the system of PDEs to a coupled system of ODEs.

A2. Initial Conditions and the Interseismic Phase

[79] We choose initial values of v and θ below steady state (that is, $v\theta/d_c < 1$) so that the fault restrengthens and slip decelerates during the first phase of integration. The initial slip velocity ($v_0 \exp \psi$) is 1.3×10^{-9} m/yr, which is comparable to a tectonic rate of 4 cm/yr. We set the initial value of χ at roughly -1 everywhere except a region of width $2L_{min}$ in which $\chi \approx -0.9$. The region of modestly elevated χ is sufficient to control the site of nucleation without biasing its evolution relative to nucleation with uniform initial conditions. Gaussian noise with a standard deviation of 0.2 is added to both ψ and χ. The noise is particularly important in slip law simulations; without it, there is no chance for asymmetric weakening and pulse formation to occur.

[80] After the initial deceleration, slip begins to accelerate while the fault is still strengthening, or in other words, the fault evolves toward steady state. When a small region reaches steady state, friction weakens and the nucleation phase begins. The slip speeds at this moment are quite small: in our simulations, they are $\sim 10^{-4}$ of the tectonic loading rate v_∞. During the deceleration and restrengthening phase, we do not integrate T because the total amount of heat generated at these low slip speeds is small and easily dissipated by diffusion. We have verified that approach by integrating the fully coupled system through this early portion of nucleation and finding that the added computational expense yields no discernible difference in solutions of T during the last 10% of the nucleation time when thermal pressurization is significant. We enable the shear heating and finite difference diffusion calculation when v_{max} is 10 times greater than the slowest point, which only occurs when a nucleation zone has begun to form. At this point, we set the temperature change to be $\Delta T = 0$ everywhere. It is possible to use an analytical solution such as equation (43) to make a more realistic estimate of the initial temperature field, but we have found that doing so does not have a discernible effect.

A3. Finite Difference Method

[81] We approximate d^2/dy^2 with a second-difference operator. We start with a diffusion grid that extends $12\sqrt{c_{th} d_c / v_{init}}$ (roughly six diffusion lengths) away from the fault. We use between 96 and 160 grid points away from the fault; the smaller value offers sufficient resolution but sometimes more grid points are necessary for the ODE solver to operate accurately. For grid point located $k\Delta y$ off the fault, the finite difference operator is given by

$$\left.\frac{\partial^2 T}{\partial y^2}\right|_k \approx \frac{T_{k-1} - 2T_k + T_{k+1}}{(\Delta y)^2} \ . \tag{A4}$$

At the fault ($k = 0$), the first derivative is prescribed (Neumann boundary condition) according to equation (11). A Taylor series expansion of T at the fault is

$$T_k = T_0 + \frac{k}{2}\left.\frac{\partial T}{\partial y}\right|_0 \Delta y + \frac{k^2}{2}\left.\frac{\partial^2 T}{\partial y^2}\right|_0 (\Delta y)^2 + \frac{k^3}{2}\left.\frac{\partial^3 T}{\partial y^3}\right|_0 (\Delta y)^3 + \mathcal{O}\left([\Delta y]^4\right) \ . \tag{A5}$$

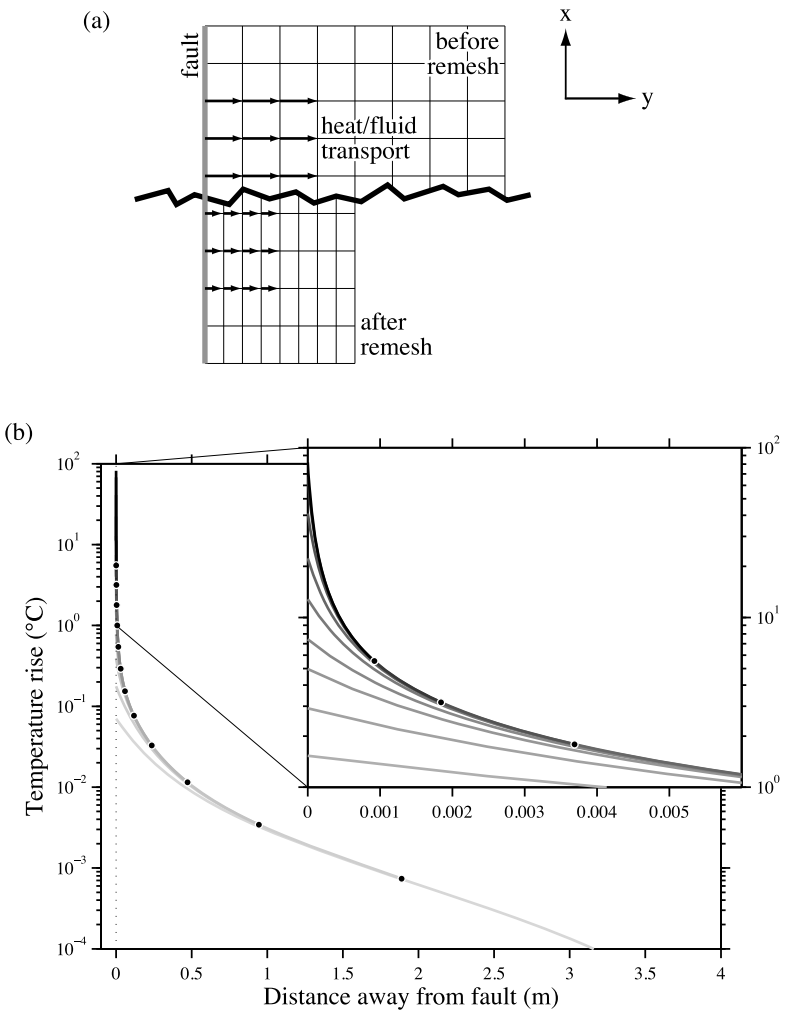

Figure A1. (a) Schematic showing finite difference grid before and after a remeshing event. (b) Temperature profiles during the simulation of Figure 6. Snapshots are immediately before remeshing events: they do not correspond to the snapshots shown elsewhere in this paper. The dots indicate the end of the finite difference domain for each profile.

By linearly combining T_1, T_2, T_3, and T_4 such that the $(\Delta y)^3$ terms cancel, we obtain

$$\left.\frac{\partial^2 T}{\partial y^2}\right|_0 \approx \frac{-7T_0 + 8T_1 - T_2}{2(\Delta y)^2} - \frac{3}{\Delta y}\left.\frac{\partial T}{\partial y}\right|_0 , \tag{A6}$$

where

$$\left.\frac{\partial T}{\partial y}\right|_0 = \frac{\tau v}{2\rho c_v c_{\text{th}}} . \tag{A7}$$

The far-field boundary condition is $\dot{T} = 0$, so for a grid of M points off the fault,

$$\left.\frac{\partial^2 T}{\partial y^2}\right|_M \equiv 0 . \tag{A8}$$

In integrating the equation of motion (20), equations (A4), (A6), and (A8) yield $\dot{T}$, and the shear heating is included in the second term of equation (A6).

A4. Remeshing

[82] Because rate- and state-dependent friction evolves over both long and short timescales, the coupled diffusion problem also must handle a corresponding range of length scales. With an explicit finite difference scheme for the diffusion equation, numerical stability requires that the size of a time step Δt be limited by grid spacing Δy according to the Courant-Friedrichs-Lewy (CFL) condition,

$$c\,\Delta t \le \frac{1}{2}(\Delta y)^2 . \tag{A9}$$

Late in nucleation, slip dramatically increases temperature over short times, and the initial FD grid is too coarse to evaluate the steep thermal gradients adjacent to the fault. Early in nucleation, however, the heating is modest and diffusion transports heat far from the fault. A fine mesh with sufficient off-fault extent would require considerable computational expense at early times, when velocity and state do

not change greatly. Therefore we start the finite difference grid with large Δy and remesh to finer values as needed.

[83] In our remeshing scheme, we maintain the same number of grid points while halving the grid spacing, which has the effect of halving the off-fault length of the diffusion grid. Values of T at new grid points (located exactly halfway between existing grid points) are found using piecewise cubic Hermite interpolation. Discarding the distal half of the temperature profile is allowable for monotonically accelerating fault slip if the time to instability is short compared to the diffusion time across the new shorter grid. This needs to be verified following the computation. Figure A1a shows schematically how the finite difference grid changes in a remeshing event. One additional constraint on remeshing is that we require $\dot{T}(y = 0)$ to be conserved during a remeshing event. To accomplish this, we adjust the new value of T_1 such that the value of equation (A6) is maintained.

[84] We select a criterion to trigger remeshing in a somewhat arbitrary manner. Through experimentation, we have found that satisfying the criterion

$$\frac{T_0 - T_1}{T_1 - T_2} < 1.3 \tag{A10}$$

works better than the more rigorous method of calculating a higher-order error term in the Taylor series expansion.

[85] Figure A1b shows an example remeshing for the simulation shown in Figure 6. Temperature profiles are shown for the final time step at each grid dimension, and the distant end of the grids are marked with dots. As mentioned in section A3, the far-field boundary condition is $\dot{T} = 0$ on the new far end of the FD grid. The fact that the far-field slope of the temperature profiles does not noticeably change over the time steps at a given grid resolution indicates that shrinking the y dimension of the finite difference grid does not bias the energy flux away from the fault via the boundary condition on $\dot{T}(y_M)$.

A5. Integration in Time

[86] With the equation of motion (20) written in terms of time derivatives and the heat transport given by finite difference approximations, the coupled system becomes a set of ordinary differential equations in ψ, χ, and T that can be integrated with existing ODE solvers. We use the ODE solver "ode45" supplied with MATLAB [*Shampine and Reichelt*, 1997], which uses an explicit Runge-Kutta method. Rate- and state-dependent friction is a stiff system (that is, at times it evolves slowly while at other times it evolves rapidly, requiring extremely small time steps) and the "ode45" solver is not designed for stiff systems. We have found that "ode45" nonetheless performs well for the coupled friction-thermal pressurization problem, especially with some modifications for more efficient memory use. It has a significant advantage over stiff system solvers such as "ode15s," which requires a Jacobian matrix to be calculated and greatly increases the code's computational overhead.

[87] **Acknowledgments.** We thank Allan Rubin for helpful suggestions on how to carefully model rate- and state-dependent frictional nucleation. Jim Dieterich's suggestion to use the variable normal stress effect proved to be invaluable. Andrew Bradley provided useful assistance with numerical methods. Comments from two anonymous reviewers were helpful in clarifying the applicability of our analysis. This work was conducted with support from National Science Foundation grant EAR-0838267, U. S. Geological Survey grants 07HQGR0015 and 08HQGR0014, and the Southern California Earthquake Center. T. Matsuzawa's contribution was supported by a JSPS Research Fellowship.

References

Ampuero, J.-P., and A. M. Rubin (2008), Earthquake nucleation on rate and state faults: Aging and slip laws, *J. Geophys. Res.*, *113*, B01302, doi:10.1029/2007JB005082.

Andrews, D. J. (2002), A fault constitutive relation accounting for thermal pressurization of pore fluid, *J. Geophys. Res.*, *107*(B12), 2363, doi:10.1029/2002JB001942.

Audet, P., M. G. Bostock, N. I. Christensen, and S. M. Peacock (2009), Seismic evidence for overpressured subducted oceanic crust and megathrust fault sealing, *Nature*, *457*, 76–78, doi:10.1038/nature07650.

Bizzarri, A., and M. Cocco (2006a), A thermal pressurization model for the spontaneous dynamic rupture propagation on a three-dimensional fault: 1. Methodological approach, *J. Geophys. Res.*, *111*, B05303, doi:10.1029/2005JB003862.

Bizzarri, A., and M. Cocco (2006b), A thermal pressurization model for the spontaneous dynamic rupture propagation on a three-dimensional fault: 2. Traction evolution and dynamic parameters, *J. Geophys. Res.*, *111*, B05304, doi:10.1029/2005JB003864.

Blanpied, M. L., D. A. Lockner, and J. D. Byerlee (1995), Frictional slip of granite at hydrothermal conditions, *J. Geophys. Res.*, *100*(B7), 13,045–13,064.

Boettcher, M. S., A. McGarr, and M. Johnston (2009), Extension of Gutenberg-Richter distribution to M_w–1.3, no lower limit in sight, *Geophys. Res. Lett.*, *36*, L10307, doi:10.1029/2009GL038080.

Bradley, A. M., and P. Segall (2010), Efficient numerical modeling of slow-slip and quasi-dynamic earthquake ruptures, *Eos Trans. AGU*, *91*(52), Fall Meet. Suppl., Abstract S23A–2115.

Carslaw, H. S., and J. C. Jaeger (1959), *Conduction of Heat in Solids*, Clarendon, Oxford, U. K.

Chambon, G., J. Schmittbuhl, and A. Corfdir (2002), Laboratory gouge friction: Seismic-like slip weakening and secondary rate- and state-effects, *Geophys. Res. Lett.*, *29*(10), 1366, doi:10.1029/2001GL014467.

Chester, F. M., and J. S. Chester (1998), Ultracataclasite structure and friction processes of the Punchbowl fault, San Andreas system, California, *Tectonophysics*, *295*, 199–221.

Chester, F. M., J. P. Evans, and R. L. Biegel (1993), Internal structure and weakening mechanisms of the San Andreas Fault, *J. Geophys. Res.*, *98*(B1), 771–786.

Cochard, A., and J. R. Rice (2000), Fault rupture between dissimilar materials: Ill-posedness, regularization, and slip-pulse response, *J. Geophys. Res.*, *105*(B11), 25,891–25,907.

Dieterich, J. H. (1979), Modeling of rock friction: 1. Experimental results and constitutive equations, *J. Geophys. Res.*, *84*(B5), 2161–2168.

Dieterich, J. H. (1992), Earthquake nucleation on faults with rate- and state-dependent strength, *Tectonophysics*, *211*, 115–134.

Dieterich, J. H. (1994), A constitutive law for rate of earthquake production and its application to earthquake clustering, *J. Geophys. Res.*, *99*(B2), 2601–2619.

Dieterich, J. H., and B. D. Kilgore (1994), Direct observation of frictional contacts: New insights for state-dependent properties, *Pure Appl. Geophys.*, *143*(1–3), 283–302.

Dieterich, J. H., and K. Richards-Dinger (2008), Characteristics of earthquake occurrence in fault systems, *Eos Trans. AGU*, *89*(53), Fall Meet. Suppl., Abstract S32A–03.

Garagash, D. I., and J. W. Rudnicki (2003), Shear heating of a fluid-saturated slip-weakening dilatant fault zone: 1. Limiting regimes, *J. Geophys. Res.*, *108*(B2), 2121, doi:10.1029/2001JB001653.

Habib, P. (1967), Sur un mode de glissement des massifs rocheaux, *C. R. Hebd. Séances Acad. Sci.*, *264*, 151–153.

Ide, S., and G. C. Beroza (2001), Does apparent stress vary with earthquake size?, *Geophys. Res. Lett.*, *28*(17), 3349–3352.

Kanamori, H., and T. H. Heaton (2000), Microscopic and macroscopic physics of earthquakes, in *Physics of Earthquakes*, *Geophys. Monogr. Ser.*, vol. 120, edited by J. B. Rundle, D. L. Turcotte and W. Klein, pp. 147–163, AGU, Washington, D. C.

Lachenbruch, A. (1980), Frictional heating, fluid pressure, and the resistance to fault motion, *J. Geophys. Res.*, *85*(B11), 6097–6112.

Lachenbruch, A., and J. H. Sass (1980), Heat flow and energetics of the San Andreas Fault zone, *J. Geophys. Res.*, *85*(B11), 6185–6223.

Lapusta, N., J. R. Rice, Y. Ben-Zion, and G. Zheng (2000), Elastodynamic analysis for slow tectonic loading with spontaneous rupture episodes on faults with rate- and state-dependent friction, *J. Geophys. Res.*, *105*(B10), 23,765–23,790.

Lee, T. C., and P. T. Delaney (1987), Frictional heating and pore pressure rise due to fault slip, *Geophys. J. R. Astron. Soc.*, *88*(3), 569–591.

Linker, M. F., and J. H. Dieterich (1992), Effects of variable normal stress on rock friction: Observations and constitutive equations, *J. Geophys. Res.*, *97*(B4), 4923–4940.

Liu, Y., and J. R. Rice (2005), Aseismic slip transients emerge spontaneously in three-dimensional rate and state modeling of subduction earthquake sequences, *J. Geophys. Res.*, *110*, B08307, doi:10.1029/2004JB003424.

Lockner, D. A., H. Naka, H. Tanaka, H. Ito, and R. Ikeda (2000), Permeability samples and strength of core samples from the Nojima fault of the 1995 Kobe earthquake, in *Proceedings of the International Workshop on the Nojima Fault Core and Borehole Data Analysis, Tsukuba, Japan, Nov 22–23 (1999)*, edited by H. Ito et al., *U.S. Geol. Surv. Open File Rep., 00-129*, 147–152.

Marone, C., and B. D. Kilgore (1993), Scaling of the critical slip distance for seismic faulting with shear strain in fault zones, *Nature*, *362*, 618–621.

Marone, C., C. B. Raleigh, and C. H. Scholz (1990), Frictional behavior and constitutive modeling of simulated fault gouge, *J. Geophys. Res.*, *95*(B5), 7007–7025.

Mase, C. W., and L. Smith (1985), Pore fluid pressures and frictional heating on a fault surface, *Pure Appl. Geophys.*, *122*, 583–607.

Mase, C. W., and L. Smith (1987), Effects of frictional heating on the thermal, hydrologic, and mechanical response of a fault, *J. Geophys. Res.*, *92*(B7), 6249–6272.

Nakatani, M. (2001), Conceptual and physical clarification of rate and state friction: Frictional sliding as a thermally activated rheology, *J. Geophys. Res.*, *106*(B7), 13,347–13,380.

Noda, H., E. M. Dunham, and J. R. Rice (2009), Earthquake ruptures with thermal weakening and the operation of major faults at low overall stress levels, *J. Geophys. Res.*, *114*, B07302, doi:10.1029/2008JB006143.

Prakash, V., and R. J. Clifton (1993), Time-resolved dynamic friction measurements in pressure-shear, in *Experimental Techniques in the Dynamics of Deformable Bodies*, vol. AMD 165, edited by K. T. Ramesh, pp. 33–48, Am. Soc. Mech. Eng., New York.

Rice, J. R. (1993), Spatio-temporal complexity of slip on a fault, *J. Geophys. Res.*, *98*(B6), 9885–9907, doi:10.1029/93JB00191.

Rice, J. R. (2006), Heating and weakening of faults during earthquake slip, *J. Geophys. Res.*, *111*, B05311, doi:10.1029/2005JB004006.

Rice, J. R., N. Lapusta, and K. Ranjith (2001), Rate and state dependent friction and the stability of sliding between elastically deformable solids, *J. Mech. Phys. Solids*, *49*, 1865–1898.

Richardson, E., and C. Marone (1999), Effects of normal stress vibrations on frictional healing, *J. Geophys. Res.*, *104*(B12), 28,859–28,878.

Rubin, A. M., and J.-P. Ampuero (2005), Earthquake nucleation on (aging) rate and state faults, *J. Geophys. Res.*, *110*, B11312, doi:10.1029/2005JB003686.

Rubin, A. M., and J.-P. Ampuero (2009), Self-similar slip pulses during rate-and-state earthquake nucleation, *J. Geophys. Res.*, *114*, B11305, doi:10.1029/2009JB006529.

Ruina, A. (1983), Slip instability and state variable friction laws, *J. Geophys. Res.*, *88*(B12), 10,359–10,370.

Segall, P. (2010), *Earthquake and Volcano Deformation*, Princeton Univ. Press, Princeton, N. J.

Segall, P., and J. R. Rice (1995), Dilatancy, compaction, and slip instability of a fluid-infiltrated fault, *J. Geophys. Res.*, *100*(B11), 22,155–22,171.

Segall, P., and J. R. Rice (2006), Does shear heating of pore fluid contribute to earthquake nucleation?, *J. Geophys. Res.*, *111*, B09316, doi:10.1029/2005JB004129.

Segall, P., A. M. Rubin, A. M. Bradley, and J. R. Rice (2010), Dilatant strengthening as a mechanism for slow slip events, *J. Geophys. Res.*, *115*, B12305, doi:10.1029/2010JB007449.

Shampine, L. F., and M. W. Reichelt (1997), The Matlab ODE suite, *SIAM J. Sci. Comput.*, *18*(1), 1–22.

Sibson, R. H. (1973), Interactions between temperature and pore-fluid pressure during earthquake faulting and a mechanism for partial of total stress relief, *Nature Phys. Sci.*, *243*(126), 66–68.

Sibson, R. H. (1986), Earthquakes and rock deformation in crustal fault zones, *Annu. Rev. Earth Planet. Sci.*, *14*, 149–175.

Sibson, R. H. (2003), Thickness of the seismic slip zone, *Bull. Seismol. Soc. Am.*, *93*(3), 1169–1178.

Sleep, N. H. (1995a), Frictional heating and the stability of rate and state dependent frictional sliding, *Geophys. Res. Lett.*, *22*(20), 2785–2788.

Sleep, N. H. (1995b), Ductile creep, compaction, and rate and state dependent friction within major fault zones, *J. Geophys. Res.*, *100*(B7), 13,065–13,080.

Suzuki, T., and T. Yamashita (2006), Nonlinear thermoporoelastic effects on dynamic earthquake rupture, *J. Geophys. Res.*, *111*, B03307, doi:10.1029/2005JB003810.

Vredevoogd, M. A., D. D. Oglesby, and S. K. Park (2007), Fluid pressurization due to frictional heating on a fault at a permeability contrast, *Geophys. Res. Lett.*, *34*, L18304, doi:10.1029/2007GL030754.

Wibberley, C. A. J., and T. Shimamoto (2003), Internal structure and permeability of major strike-slip fault zones: The Median Tectonic Line in Mie Prefecture, Southwest Japan, *J. Struct. Geol.*, *25*, 59–78.

Zoback, M., S. Hickman, and W. Ellsworth (2010), Scientific drilling into the San Andreas Fault zone: Overview and research opportunities, *Eos Trans. AGU*, *91*(22), 197–199, doi:10.1029/2010EO220001.

T. Matsuzawa, National Research Institute for Earth Science and Disaster Prevention, 3-1 Tennodai, Tsukuba, Ibaraki 305-0006, Japan.

S. V. Schmitt and P. Segall, Department of Geophysics, Stanford University, 397 Panama Mall, Stanford, CA 94305, USA. (schmitt@stanford.edu)